

# 1 A hierarchical atlas of the human 2 cerebellum for functional precision mapping

3 Caroline Nettekoven<sup>1,2,\*</sup>, Da Zhi<sup>1,2</sup>, Ladan Shahshahani<sup>1</sup>, Ana Luísa  
4 Pinho<sup>1,2</sup>, Noam Saadon-Grosman<sup>3</sup>, Randy Lee Buckner<sup>3</sup>, and Jörn  
5 Diedrichsen<sup>1,2,4,\*</sup>

6 <sup>1</sup>Western Institute for Neuroscience, Western University, London, Ontario, Canada

7 <sup>2</sup>Department of Computer Science, Western University, London, Ontario, Canada

8 <sup>3</sup>Harvard University, Cambridge, US

9 <sup>4</sup>Department of Statistical and Actuarial Sciences, Western University, London, Ontario,  
10 Canada

11 \*Corresponding authors: Caroline Nettekoven, [cr.nettekoven@gmail.com](mailto:cr.nettekoven@gmail.com); Jörn  
12 Diedrichsen, [jdiedric@uwo.ca](mailto:jdiedric@uwo.ca)

## 13 ABSTRACT

The human cerebellum is activated by a wide variety of cognitive and motor tasks. Previous functional atlases have relied on single task-based or resting-state fMRI datasets. Here, we present a functional atlas that integrates information from 7 large-scale datasets, outperforming existing group atlases. The new atlas has three further advantages: First, the atlas allows for precision mapping in individuals: The integration of the probabilistic group atlas with an individual localizer scan results in a marked improvement in prediction of individual boundaries. Second, we provide both asymmetric and symmetric versions of the atlas. The symmetric version, which is obtained by constraining the boundaries to be the same across hemispheres, is especially useful in studying functional lateralization. Finally, the regions are hierarchically organized across 3 levels, allowing analyses at the appropriate level of granularity. Overall, the new atlas is an important resource for the study of the interdigitated functional organization of the human cerebellum in health and disease.

Keywords: Cerebellum, Brain Atlasing, Hierarchical Bayesian model, Functional brain parcellation, task-based fMRI, resting-state fMRI

## 14 INTRODUCTION

15 Decades of neuroimaging have shown cerebellar activation in a broad range of tasks, including motor,  
16 social, and cognitive tasks - yet its contribution to these different functions remains elusive [1, 2]. A  
17 major obstacle to understanding the cerebellar contribution is that the cerebellum consists of a mosaic of  
18 functional regions, specialized for distinct roles [3]. It is still common to use the anatomical subdivision  
19 into different lobules [4, 5] to define regions of interest, even though lobular boundaries do not align with  
20 boundaries in functional specialization [3].

21 There are several existing maps based on resting-state or task-based functional Magnetic Resonance  
22 Imaging (fMRI) data [6, 7, 3] that parcellate the cerebellum into functional regions. These functional  
23 atlases outperform anatomical parcellations at predicting functional boundaries on an independent task  
24 set, with a task-based parcellation based on a large multi-domain task battery (MDTB) being particularly  
25 powerful [3]. Nonetheless, parcellations based on single datasets usually show some distinct weaknesses:  
26 For example, the MDTB parcellation [3] does not delineate the foot or mouth motor region very well,  
27 likely because of the absence of those movement types from the task set. Any single dataset and analysis  
28 approach will necessarily emphasize some features over others. To address these shortcomings, we have  
29 recently developed a Bayesian Hierarchical method that combines information across datasets into a  
30 single parcellation [8]. In this study, we apply this model to seven large task-based datasets to derive a  
31 novel cerebellar functional atlas.

32 Another important limitation of existing group atlases is that they ignore the large inter-individual  
33 variability in functional brain organization [9, 10, 11, 12, 13]. This problem is particularly relevant

34 for the cerebellar cortex, where many functionally heterogeneous regions are packed into a relatively  
35 small volume [14, 3, 15]. Multiple groups have therefore pursued a precision mapping approach, using  
36 localizing data to define functional regions at the individual level [10, 11, 12, 15]. To enable such precise  
37 and fine-grained analysis, the new atlas is based on a probabilistic framework, which allows the user to  
38 use even limited individual data to optimally tailor the atlas to an individual [8, 16]. We evaluated this  
39 approach carefully by showing the utility of the personalized parcellation at predicting boundaries and  
40 functional specialization in the same individual in different tasks, as compared to both the group atlas,  
41 and a parcellation solely based on individual data.

42 The cerebellum plays a key role in lateralized functions (i.e., language; [17]) and shows lateralized  
43 developmental trajectories [18]. The study of lateralization, however, is complicated by existing functional  
44 atlases, as they have asymmetric boundaries with ambiguities in correspondence between left  
45 and right regions. We therefore developed a version of the atlas with symmetric boundaries and matching  
46 hemispheric parcel pairs. Importantly, we did not constrain the functional profiles to be the same across  
47 hemispheres, enabling us to study functional lateralization. The comparison to an asymmetric version of  
48 the atlas also allowed us to assess whether this symmetry constraint is adequate, or to what degree the  
49 spatial organization is truly asymmetric.

50 Finally, questions about cerebellar function will benefit from being tested at different levels of  
51 granularity. For many anatomical and patient studies, it is often most appropriate to summarize measures  
52 in terms of broad functional domains (e.g., motor vs. social-linguistic-spatial regions), whereas more  
53 detailed functional studies require the definition of finer region distinctions (e.g., separate hand, foot,  
54 and tongue regions within the motor domain or separation between social and linguistic domains). We  
55 therefore created the atlas with a hierarchical organization of functional regions where the boundaries of  
56 the broad domains remain the same at each level of granularity.

## 57 RESULTS

### 58 Different fMRI datasets reveal a similar, but not identical, cerebellar organization

59 A common functional atlas across different datasets only makes sense, if we assume that there is a robust  
60 functional organization that remains the same across tasks. However, the cognitive state of the brain (rest  
61 or specific tasks) likely influences how different functional regions work together. Therefore, parcellations  
62 based on different datasets may highlight different functional boundaries. As a first step, we therefore  
63 sought to characterize similarities between parcellations based on single datasets, using task-based and  
64 resting-state data. We trained our probabilistic parcellation model [8] on seven task-based and one  
65 resting-state datasets (Supplemental Table. 1) in isolation and then compared the resultant parcellations  
66 (Fig. 1a).

67 The parcellations overall showed clear similarities, but also some dataset-specific differences. A  
68 smooth boundary between motor regions in lobule I-VI and cognitive regions in lobule VII was present in  
69 all parcellations (e.g. between the magenta and pink regions in MDTB and Demand dataset in lobule VI).  
70 On the other hand, the ability to distinguish regions within motor and cognitive regions differed between  
71 datasets. For example, the somatotopic dataset only tested individual body movements, and therefore  
72 resulted in a clear somatomotor map, but did not delineate cognitive regions in lobule VII well, as can  
73 be seen by the fragmented pattern in Crus I/II and lobule IX. In contrast, the Demand dataset delineated  
74 regions involved in working memory and executive functions, but did not lead to a clear somatomotor  
75 map. Parcellations based on resting-state data (HCP) showed consistent boundaries in regions related to  
76 the default network (lobules VII) but appear to delineate other regions (e.g. motor) less finely.

77 To quantify these similarities, we calculated the adjusted Rand Index (ARI) between parcellations at  
78 different levels of parcel granularity (10, 20, 34, 40 and 68 regions). The indices were averaged across  
79 granularities and normalized by the within-dataset ARI (Fig. 1c, see methods). Overall, the resultant  
80 reliability-adjusted ARIs were positive across all dataset pairs (One-sample t-test of the between-dataset  
81 ARIs averaged across granularities  $t_{27} = 17.885, p = 1.696 \times 10^{-16}$ ), indicating that there are clear  
82 commonalities across all different task and resting state datasets [20, 10, 21].

83 To assess the similarity of the resulting parcellations better, we visualized the reliability-adjusted  
84 ARIs using multi-dimensional scaling (Fig. 1b). Unsurprisingly, task-based datasets that test similar  
85 task domains (i.e., working memory and multi-demand dataset) resulted in similar parcellations. The  
86 Somatotopic and the resting-state (HCP) parcellation occupied two other, opposing poles in the space of  
87 parcellations.

88 Parcellations based on datasets that included a large range of cognitive tasks (MDTB, MDTB-  
89 Highres, and IBC) occupied a middle position, suggesting that such parcellations can well capture stable  
90 features of functional boundaries across tasks. Indeed, when we compared the ARI for each specific  
91 task-based parcellations, we found that they were more similar to the parcellation derived from the  
92 MDTB dataset than to one derived from the HCP dataset (paired t-test:  $t_{149} = 9.605, p = 2.672 \times 10^{-17}$ ;  
93 Fig. 1d). Testing each set of task-based parcellations separately confirmed that all, except for the  
94 Nishimoto parcellations ( $t_{24} = -0.838, p = 0.410$ ) were significantly more similar to the MDTB than  
95 the HCP (resting-state) parcellations (MDTB-Highres:  $t_{24} = 16.404, p = 1.523 \times 10^{-14}$ ; IBC:  $t_{24} =$   
96  $3.513, p = .0017$ ; WM:  $t_{24} = 4.727, p = 8.318 \times 10^{-5}$ ; Demand:  $t_{24} = 3.262, p = .0033$ ; Somatotopic:  
97  $t_{24} = 12.538, p = 5.015 \times 10^{-12}$ ). As indicated by the opposing poles occupied by Somatotopic dataset  
98 and HCP resting-state dataset (Fig. 1b), this difference was largest for the Somatotopic dataset, suggesting  
99 that rest and single-limb movements reveal quite dissimilar boundaries.

100 In sum, this analysis shows that the resting-state parcellation captures many task-based boundaries,  
101 but also differs from a parcellation that delineates somatotopic motor regions. This is in line with previous  
102 observations that resting-state data do not always reveal motor regions of the cerebellum clearly [7, 22].  
103 In practice we found that the inclusion of resting-state data into the fused atlas tended to prevent a clear  
104 delineation of somatomotor regions. For the final atlas we therefore decided to rely on task-based data  
105 only given the goal here of comprehensively mapping motor and non-motor cerebellar regions.

### 106 **Dataset fusion improves prediction of functional boundaries**

107 Our Hierarchical Bayesian Parcellation framework [8] allows for data fusion by modelling each dataset  
108 separately and then combines them iteratively into a common group atlas. In this process, each dataset is  
109 weighted by a measure of its reliability (see methods, Hierarchical Bayesian parcellation framework).

110 To verify that the fusion of datasets through our framework systematically improved on single-dataset  
111 parcellations, we adopted a leave-one-dataset-out approach. We trained the fusion parcellation on all  
112 task-based datasets except one and tested its ability to predict the functional boundaries within that left-out  
113 dataset. This ability was quantified using the Distance-Controlled Boundary Coefficient (DCBC) which  
114 compares the correlation between within-parcel voxel-pairs to the correlation between voxels-pairs across  
115 a boundary, while controlling for spatial distance [23], with higher values indicating better performance.  
116 We found that the fused group atlas outperformed single dataset parcellations averaged across granularities  
117 ( $t_{110} = -4.466, p = 1.936 \times 10^{-5}$ ; Fig. 1e left).

118 In addition to providing a winner-take all group map, our framework can also provide individual  
119 parcellations by integrating subject-specific data (see methods: individual precision mapping). This ability  
120 critically depends on the group atlas not only having appropriate boundaries, but also quantifying the  
121 uncertainty across participants adequately. We found that individual parcellations based on the fused atlas  
122 outperformed those derived from single dataset ( $t_{110} = -2.564, p = .0171$ ; Fig. 1e right), confirming the  
123 superiority of the fused atlas, both when using a winner-take-all projection or a probabilistic parcellation  
124 to derive individual maps [8].

### 125 **Comparing symmetric and asymmetric atlases**

126 To enable the study of hemispheric specialization, we initially constrained our atlas to have spatially  
127 symmetric regions across the left and right cerebellar hemispheres, while allowing different functional  
128 profiles. To determine how much this constraint forced the group map to deviate from the true functional  
129 organisation, we also estimated an asymmetric version of the atlas without using the symmetry constraint  
130 (see methods, Symmetry constraint).

131 We compared the ability of the asymmetric and the symmetric atlas to predict functional boundaries,  
132 again adopting a leave-one-dataset-out approach. For the group DCBC, we found a small, but significant  
133 difference between the asymmetric and symmetric atlas across levels of granularity (10-68 regions;  
134  $t_{110} = -2.344, p = .0201$ ) (Fig. 1B). This advantage was larger at the individual level ( $t_{110} = -5.023, p =$   
135  $1.981 \times 10^{-6}$ ). Overall, however, the predictive power of the symmetric atlas was only 5% (group) or  
136 14% (individual) smaller than the asymmetric versions. Given the many practical uses of the symmetric  
137 atlas for controlling for region size and location in lateralization studies, we provide both symmetric and  
138 asymmetric versions of the final atlas.

### 139 **Basemap for hierarchical atlas outperforms existing parcellations**

140 Instead of choosing a fixed number of regions, we used three nested levels of resolution, linked in a  
141 hierarchical scheme. This allows the user to analyze their data at different levels of granularity in a  
142 consistent fashion. To decide on the “base map” of this hierarchy, we examined the predictive performance  
143 of the fusion atlas across the tested levels of granularity at the group and individual levels (Fig. 1f). We  
144 found that the performance of the group map saturated early, reaching its best value at 20 regions. However,  
145 this peak was not significantly different from the finest granularity of 68 regions ( $t_{110} = 2.783, p = .0063$ ).  
146 In contrast, the ability to predict boundaries in the individual increased monotonically, with the finest  
147 granularity outperforming the next lower granularity of 40 regions ( $t_{110} = 7.584, p = 1.143 \times 10^{-11}$ ). We  
148 therefore based the hierarchical atlas on the map with the finest granularity of 68 functional regions.

149 The fused atlas based on all datasets significantly outperformed existing parcellations in predicting  
150 boundaries tested on all datasets. Across all subjects of all evaluation datasets, both the symmetric and  
151 the asymmetric atlas base map resulted in a higher average DCBC than existing anatomical (Lobular:  
152 [5]), task-based (MDTB: [3], and resting-state parcellations (7 and 17 regions: [7]; 10 regions: [6]), all  
153  $t_{110} > 3.545, p < 5.788 \times 10^{-4}$  (see Supplemental Fig. S1)

154 We then clustered the 34 regions per hemisphere of the basemap into 16 regions per hemisphere  
155 according to the functional similarity between regions (see methods: parcel similarity and clustering).  
156 Finally, we organized these 16 regions into 4 broad functional domains. Based on their functional  
157 activation profiles, we denoted these four functional domains as motor (M), action (A), multi-demand (D),  
158 and social-linguistic-spatial (S) (Fig. 2c). At the medium level, we numbered the regions within each  
159 domain from medial to lateral (Fig. 2d). Finally, the finest level was annotated with a lowercase letter  
160 (a-d). In the following description of the regions, we will focus on the medium level, as it provides a good  
161 compromise between precision and succinctness.

### 162 **Characterization of functional regions**

163 Each functional region is characterized by its response profile across datasets and its spatial distribu-  
164 tion across individuals. In describing the functional profile, we focused on responses estimated from  
165 subject-specific regions in the MDTB dataset (see methods: Functional profiles for the MDTB dataset),  
166 supplemented by more domain-specific datasets for the motor and demand regions (Somatotopic, Demand,  
167 WM).

#### 168 ***Motor regions***

169 Regions that exhibited a clear preference for movements of a specific body part were grouped into the  
170 motor domain. All regions had a superior (lobules I-VI) and an inferior (lobule VIII) aspect. We also  
171 found a third representation of these body-part-specific regions in the posterior vermis, consistent with  
172 recent results at the individual subject level [22].

173 M1 encompassed the oculomotor vermis, which responded most strongly to saccades (Fig. S2). Even  
174 when correcting for the number of saccades, the area was further activated when participants had to read  
175 text (Theory-of-Mind), watch a movie (animated movie), or search for visual stimuli (spatial map and  
176 visual search), likely due to the attentional demands of these tasks. Previous work has shown that this  
177 region also has a clear retinotopic organization [24]. M2 comprises a lateral and a vermal part. The lateral  
178 section showed strong responses to tongue movements in the somatotopic dataset. In contrast, the vermal  
179 component was activated by multiple different bodily movements, but otherwise was functionally most  
180 similar to the lateral M2. The M3 regions were selectively activated movement of the ipsilateral hand  
181 (Supplemental Fig.S2). Finally, M4 was most activated by movements of the lower body, including flexion  
182 and extension of the foot (Highres-MDTB), as well as contraction of the gluteal muscles (Somatotopic).

#### 183 ***Action regions***

184 Directly adjacent to the motor regions lie the action regions, which were activated during action observation  
185 and motor imagery tasks. A1 and A2 both comprised spatially separate superior and inferior sections. A1  
186 can be found medially to the hand region in lobule VI and at the border of VIIIa/VIIIb. A2 lies laterally  
187 adjacent to the superior hand region M3, and at the border of lobule VIIIa/VIIIb. In contrast, A3 primarily  
188 occupies the inferior cerebellum (Fig. S3), located at the border of lobules VIIIa/VIIIb.

189 Although both motor and action regions activated during movement execution, only the action regions  
190 activated when observing actions without execution: In the MDTB dataset, they showed strong responses  
191 to an action observation task (video actions in Fig. S2). A1 appeared to be particularly involved where

192 spatial simulation is required (strong responses during spatial map and mental rotation tasks). Meanwhile,  
193 A2 seems to be a classic action observation region, with little response to tasks that do not involve action  
194 observation or execution. In contrast, A3 was also activated during imagined movements (motor imagery).

### 195 **Multiple-demand regions**

196 Tasks involving executive control, including updating, shifting and inhibition, consistently activated  
197 regions in lobules VI and VII. Based on work by Duncan et al. [25], we labelled these regions the  
198 multi-demand domain (D for short). D1 occupied the most medial portion of Crus I and II. Further out in  
199 the hemispheres, the demand region formed a "shell" around the more central social-linguistic-spatial  
200 domain (Fig. S4b and Fig. S5). Here, D3 formed the outermost layer and D2 the innermost, with D1  
201 being interspersed between. The regions (especially D2) also had a repeated representation in lobule IX  
202 (Fig. S3). This is consistent with a 3-fold representation [7]. Intriguingly, we found also a vermal section  
203 of D3, both in lobule IV and IX. D4 was the smallest identified region. Functionally most similar to D1, it  
204 occupied the most lateral portion of the demand regions.

205 Consistent with the characteristics of the cortical multi-demand system [26], all regions showed  
206 significant activation during executive tasks (n-back, switch and stop tasks), and increased activity  
207 especially with high difficulty. Nonetheless, there was some functional specialization across the regions.  
208 In the MDTB dataset, D1 appeared to be involved strongly in spatial tasks, such as the mental rotation,  
209 and spatial map task. D1 and D4 were strongly engaged in the n-back task. In contrast, D2 and D3 were  
210 specifically activated by the digit span task tested in the WMFS data set - with D2 more active during  
211 backwards recall and D3 showing strong increases with working memory load.

### 212 **Social-linguistic-spatial regions**

213 The regions in hemispheric lobules Crus I and Crus II, located laterally to the D1 region, were activated by  
214 tasks involving social and linguistic processes. They also showed high activity during rest, consistent with  
215 the description of this area as the cerebellar node of the default network [7]. We identified four regions,  
216 each spanning both sides of the horizontal fissure, with S1 being the most medial and S4 most lateral  
217 (Fig. 2). S3 overlapped substantially with S2 and S4 and therefore could only be reliably differentiated  
218 from these two regions at the level of the individual (see 5a). In the volume (Supplementary Fig. S4)  
219 S1 occupies the depth of the horizontal fissure, and S4 the most lateral tips of Crus I and II. A third  
220 representation of S2 and S4 can be found in lobules IX. S1 and S2 also occupy sections in the inferior  
221 vermis (VIIIb and IX, Supplementary Fig. S4). While all regions shared some overall similarity in their  
222 response profile, there were clear inter-regional and inter-hemispheric differences. The mean evoked  
223 responses for the MDTB dataset (Supplementary Fig. S2) showed right S1 to be primarily involved in  
224 linguistic processing, with highest activation during verb generation. S2 was strongly engaged in social  
225 processing, with highest activity during a theory-of-mind task on the right and during an animated movie  
226 on the left. S2, S3, and S4 showed high levels of activity during rest. S4 and S5 appeared to be particularly  
227 involved in imagination and specific forms of self-projection (Supplementary Fig. S6a,b), showing the  
228 highest activation during the spatial and the motor imagery tasks, which require the participant to imagine  
229 themselves walking through their childhood home and playing a game of tennis, respectively. In contrast  
230 to S4, S5 was also active during a spatial working memory task (Spatial Map) and did not appear to  
231 be engaged in linguistic processes (Verb generation)(Supplementary Fig. S6c,d). S5 was also activated  
232 by the action observation task, such that it functionally takes up an intermediate position between the  
233 social-linguistic-spatial and action domain. When comparing these regions to the recently described  
234 subdivision of the default network [27], S4 and S5 appear more similar to default network A (associated  
235 with remembering and scene construction), and S2-S3 to default network B (theory of mind) .

### 236 **Cerebral connectivity patterns characterize distinct regions**

237 The cerebellum does not work in isolation - indeed, given the uniform cyto-architecture of the cerebellum,  
238 functional specialization arises from the different patterns of connectivity (REF?). We therefore character-  
239 ized each cerebellar region by determining the areas of the cerebral cortex that most likely provide input  
240 to this area. To do so, we estimated an effective connectivity model, aiming to explain the data in each  
241 cerebellar voxel as a linear combination of cortical regions [28]. For the task-based dataset, we used the  
242 condition-averaged profiles, for the resting-state data, the preprocessed time-series. We fitted the models  
243 individually per subject and dataset. To validate these connectivity models, we tested them in how well  
244 they could predict the cerebellar activity patterns for each other dataset, using only the corresponding

245 cortical activity patterns (see methods: Cortical connectivity).

246 The average correlation between the predicted and the observed activity patterns (Fig. 3a) were  
247 significantly higher than zero for all training / test combinations. One notable exception was the model  
248 estimated on the Somatotopic dataset, which generally performed more poorly in predicting the other  
249 data sets. Connectivity models generally showed the highest predictive accuracy on the dataset they were  
250 trained on, even though this evaluation was cross-validated across subjects.

251 Averaged over all evaluation datasets (Fig. 3b), the model trained on the MDTB dataset performed best  
252 - with the other models being nearly equivalent in their performance (with the exception of Somatotopic  
253 dataset). To fuse across datasets, we simply averaged the connectivity weights across models. We found  
254 that average prediction performance was slightly better if it did not include the HCP dataset (.396 vs. .394,  
255  $t_{102} = -1.51, p = 0.1349$ ). The final Fusion model (last bar in Fig. 3b) significantly outperformed the  
256 best individual connectivity model (MDTB,  $t_{102} = -7.340, p = 5.322 \times 10^{-11}$ ). Taking into account the  
257 noise ceiling of this prediction given by the reliability of the cerebellar and the cortical data (see methods:  
258 Cortical connectivity), the model achieved a prediction accuracy of  $R = 0.6840$ , meaning that it predicted  
259 on average 47% of the explainable variance.

260 The weights of these connectivity models for each individual region (Supplemental Figure S7, S8,  
261 S9) clearly showed connectivity with the expected cerebral regions in the contralateral hemisphere. For  
262 example, the left cerebellar hand region showed the highest connectivity with the hand region of the right  
263 primary motor cortex and somatosensory cortex, and vice versa for the right cerebellar hand region (Fig.  
264 S7c).

265 To summarize these weight maps in terms of standard cortical networks, we averaged the weights  
266 within the 15 resting-state networks described in [29] (3c). This analysis showed the expected connectivity  
267 between M1 and visual and dorsal attention networks, between M2-M3 and the Somatomotor and premotor  
268 networks, D1-D4 to the dorsal Attention network A and control networks, and S1-S5 to language and  
269 default networks.

## 270 **Functional lateralization and boundary asymmetry**

271 The symmetric version of our atlas forced the boundaries between parcels to be the same across hemi-  
272 spheres. Nonetheless, the functional profiles for the left and right parcels were estimated separately  
273 (see methods: Symmetry constraint). Therefore, hemispheric differences in functional specialization  
274 were captured by the model. To investigate these differences, we correlated the functional profiles of  
275 corresponding left and right voxels (Fig. 4c). We observed low functional correlations between left and  
276 right hand regions (M3). This was mainly caused by task sets that isolated left- vs. right-hand movements.  
277 Such task-dependence can be clearly seen in the foot motor region (M4), which appear functionally  
278 symmetric in the MDTB-Highres dataset, which included bilateral foot movements, and functionally  
279 asymmetric in the somatotopic dataset included separate left and right movement conditions S10).

280 In contrast, the multi-demand regions consistently show high functional correlations across left and  
281 right hemispheres for all datasets, even though the task sets included different executive functions and  
282 working memory tasks, using verbal and non-verbal material. While there might be some functional  
283 lateralization within this domain, our results suggest that their response profiles are largely symmetric and  
284 that it may be difficult to find strongly lateralized tasks in this functional domain. In contrast, the social-  
285 linguistic-spatial regions showed much lower functional correlations with substantial differences between  
286 left and right response profiles. Therefore, some functions are clearly lateralized in the cerebellum,  
287 reflected in different functional profiles for left and right regions.

288 Additionally, it is also possible that boundaries between functional regions themselves are asymmetric.  
289 We therefore estimated an asymmetric version of the atlas with the same functional profiles per region, but  
290 without the constraint on symmetry. Overall, the asymmetric atlas was similar to the symmetric atlas (Fig.  
291 4a). However, closer inspection revealed some key differences between the left and right hemispheric  
292 parcels of the asymmetric atlas, with the biggest difference observed among the social-linguistic-spatial  
293 and multiple-demand regions. When we compared the region size between the left and right regions in  
294 the asymmetric atlas (supplementary Fig. S11), S3 and S4 had larger regions on the right, while S2, A2,  
295 and D1 were bigger on the left.

296 Finally, we calculated an index of boundary symmetry (see methods: Boundary symmetry) by  
297 correlating the parcel probabilities from the asymmetric and symmetric atlas. We found high boundary  
298 symmetry in motor and demand regions and low boundary symmetry in social-linguistic-spatial regions.

299 Specifically, among the motor regions the oculomotor vermis M1 and the hand region M3 (Fig. 4c) showed  
300 high boundary symmetry. All demand regions showed high boundary symmetry with the exception of D2.  
301 In the social-linguistic-spatial regions, we observed generally low boundary symmetry, indicating that for  
302 these regions an asymmetric atlas may be most appropriate.

### 303 **Individual precision mapping through integration of localizer data**

304 The fusion atlas reveals several finely inter-digitated regions that have not been well described before  
305 and that have only been localized at the single-subject level using large quantities of individual data [15].  
306 However, with the probabilistic framework, the atlas can be used to identify these regions in individual  
307 participants even with more limited data. In this section, we will describe the approach of personalizing  
308 the atlas to individuals, i.e., using the atlas for precision mapping [10, 11, 12].

309 We first characterized the spatial pattern of inter-individual variability to understand where in the  
310 cerebellum individual localization would offer the greatest utility. For each voxel, we calculated the  
311 Pearson's correlation between the functional profiles of all possible pairs of subjects in the MDTB  
312 dataset (methods:Inter-Individual variability). While motor regions showed consistent functional profiles  
313 across subjects (e.g. hand regions M3 and eye regions M1 in Fig. 5b), the social-linguistic-spatial  
314 regions were more variable. Only voxels in the core of the S1 region were relatively consistent across  
315 individuals; the lateral regions, and especially the boundary to the multi-demand regions demonstrated  
316 large inter-individual variability. Consistent with the heightened inter-individual variability in the social-  
317 linguistic-spatial regions, our atlas shows considerable overlap in the group probability maps for region S1  
318 and S2 (Fig. 5c). Hence, the study of these regions in Crus I and II and their differentiation from demand  
319 regions will benefit most from precision mapping of individuals.

320 For individual functional localization, a common approach is to acquire functional data from the  
321 individual to define individual regional boundaries [30, 31, 32]. However, a substantial amount of  
322 functional data is necessary for deriving a parcellation that performs convincingly better than a group map  
323 [8, 14, 3]. We quantified this problem here by using 10min-160min of imaging data from the first session  
324 of the MDTB data set to derive individual parcellations. We then evaluated these parcellations on how  
325 well they separated functional regions (DCBC, higher DCBC indicating better separation; Fig.5d) and  
326 predicted the functional profiles (prediction error, lower error indicating better prediction; Fig. 5e). We  
327 found that 20 min of individual data were necessary to be just as good as our new symmetric group atlas,  
328 and 40 min to significantly outperform the group map on both criteria (DCBC:  $t_{23} = 2.981, p = 0.0067$ ,  
329 Prediction error:  $t_{23} = -2.869, p = 0.0087$ ).

330 The probabilistic framework, however, allowed us to optimally combine evidence from the individual  
331 data with the probabilistic group map (see methods: Individual precision mapping). The final estimate of  
332 the model using only 20 min of functional localization data outperformed both the individual data (DCBC:  
333  $t_{23} = 11.468, p = 5.43 \times 10^{-11}$ ; Prediction error:  $t_{23} = -9.098, p = 4.414 \times 10^{-9}$ ) and the group map  
334 ( $t_{23} = 3.395, p = 0.0025$ ). The integrated estimate even improved individual parcellations based on as  
335 much as 160 mins of data (DCBC:  $t_{23} = 5.838, p = 5.989 \times 10^{-6}$ , Prediction error:  $t_{23} = -3.798, p =$   
336  $9.288 \times 10^{-4}$ ). Thus the new atlas offers both the advantage of a consistent group map, as well as the  
337 possibility to obtain precision individualized mapping of brain organization.

## 338 **DISCUSSION**

### 339 **Summary**

340 In this study, we developed a comprehensive functional atlas of the human cerebellum featuring several  
341 important advances: First, using a Hierarchical Bayesian Model, we integrated data across seven large task-  
342 based datasets, thereby achieving a more complete coverage. The new group atlas outperforms existing  
343 task-based [3] and resting-state [7] atlases in predicting functional boundaries across functional domains.  
344 Second, by enforcing boundary symmetry but letting functional responses vary between hemispheres, our  
345 symmetric atlas version is particularly suited to study functional lateralization in the cerebellum. Third,  
346 the atlas is hierarchically organized, allowing for a consistent description of the cerebellum at different  
347 levels of granularity. Finally, the probabilistic group atlas can be combined with a short localizer scan to  
348 improve functional precision mapping of individuals. As compared to the existing winner-take-all group  
349 atlases, this new approach paves the way to a detailed analysis of small subregions in the future.

### 350 **Three-fold organization of the human cerebellum**

351 Consistent with previous studies [7, 33, 15], we found overall a three-fold spatial organization of the  
352 cerebellum. For most regions, we found a primary representation located between lobule I and Crus I, a  
353 secondary representation between lobule Crus II and lobule VIIIb, and a tertiary representation in lobule  
354 IX or X. The ordering of the regions was mirrored around the horizontal fissure, such that the demand  
355 region formed a shell around the social-linguistic-spatial regions, and the action and motor regions a shell  
356 around the demand regions. While regions S2-S4 appeared on the flatmap [19] to be spatially contiguous,  
357 the volumetric view revealed S4 that these regions too have anatomically distinct primary and secondary  
358 representations, separated by the horizontal fissure. This observation exemplifies the importance of  
359 considering how regions are distributed on a fully unfolded cerebellar cortical sheet [34] instead of solely  
360 relying on the crude approximation that is offered by our flatmap visualization [19].

361 The group atlas also shows a third representations of cognitive regions in lobule IX. No third motor  
362 representation was found in the cerebellar hemispheres. Instead, a third representation of the motor  
363 regions in the inferior vermis has recently been described at the individual level using deep phenotyping  
364 approaches [22]. Our atlas, which included these data within its training set, now clearly shows this  
365 representation both at the group and the individual level S3.

366 Damage to the primary motor representations leads to more severe deficits than damage to the  
367 secondary motor representation [35]. Based on this observation, it has been speculated that there are  
368 functional differences between the three representations [33]. So far, however, a definite demonstration of  
369 distinct response profiles among the three representations has remained elusive. Two lines of evidence cast  
370 doubt on a strong functional dissociation between these representations. First, our analysis of functional  
371 regions generally grouped the three representations together, implying a significant degree of shared  
372 functional profiles across datasets. Second, tracing studies have shown that a single axon from the inferior  
373 olive can branch into multiple climbing fibers [36] and innervate different regions in non-contiguous  
374 lobules [37]. Similarly, most ponto-cerebellar mossy fibres project to multiple lobules [38]. This suggests  
375 that all three representations, despite their spatial separation, may receive very similar, or even shared,  
376 climbing fiber and mossy fiber inputs. Therefore, it is not clear whether the multiple representations of the  
377 same functional region can be functionally distinguished. To facilitate further investigations, we provide  
378 an atlas version, in which each region is subdivided into a superior (lobule I - Crus I), inferior (Crus II -  
379 VIIIb), tertiary (lobule IX - lobule X), and vermal sections (vermis VII - vermis X). With one exception  
380 (S5), this subdivision separates the spatially non-contiguous aspect of each region.

### 381 **New functional insights**

382 Although the spatial pattern of most regions adheres to a three-fold organization, our new atlas reveals that  
383 several regions deviate from this principle, suggesting a more complex cerebellar functional organization.  
384 First, not all functional regions have all three representations, for example A3 and S5 only have an inferior  
385 representation, whereas M1 only has a superior representation (supplementary Fig. S3a). Second, some  
386 regions with a primary and secondary representations are spatially connected in the volume (e.g., S1,  
387 supplementary Fig. S3a). Future neuroimaging studies might reveal a parsimonious organization or more  
388 spatial complexity, as has been suggested by intensive within-individual mapping [15].

389 Furthermore, while our atlas confirms the well-known functional regions of the cerebellum, it also  
390 uncovers regions that have not been reported or only recently identified. We describe two new regions  
391 in lobules VIII and IX, notably A3 which is engaged during spatial simulation and S5 which activates  
392 when constructing an imagined scene or engaging in specific forms of self-projection . Furthermore, the  
393 atlas revealed 5 medial-to-lateral organized regions in Crus I and II. A similar detailed subdivision has  
394 only been achieved at the individual level using several hours of scan time [27, 15]. This work showed  
395 that the default network can be divided into two parts, one that is associated with remembering and scene  
396 construction (network A), the other that is associated with mentalizing (network B). Our atlas captures this  
397 distinction, with S4 showing some correspondence with default network A, and S2 and S3 with default  
398 network B.

399 However, it is not clear a-priori that there should be 1:1 correspondence between the regions identified  
400 in this atlas and cerebral resting-state networks. Our atlas is based on data that is task-based and comes  
401 from the cerebellum only. It therefore offers a different and complementary approach to resting-state  
402 atlases, in which the networks are defined on the cerebrum, and the cerebellum subsequently labeled  
403 according to the best-matching network [7].



## 404 **Individual precision mapping**

405 Studying finely inter-digitated regions is difficult when using group-level atlases. Inter-individual vari-  
406 ability is generally high in the cerebellum [39], and our analysis (Fig. 5d) shows that the location and  
407 arrangement of the multi-demand and social-linguistic-spatial regions are especially variable across indi-  
408 viduals. High inter-individual variability has been a long-standing finding for language regions. Despite  
409 this variability, the spatial pattern of the language network, its degree of lateralization and responsiveness  
410 are relatively stable within individuals over time [40, 41]. These results stress the importance of using an  
411 individualized approach when studying cognitive regions of the cerebellum [42, 43, 44].

412 The classic approach to individual localization is to run a short localizer scan (often 10 minutes) [31],  
413 based on the assumption that these individual-level boundaries reflect the subject's organization better  
414 than boundaries defined by a group map, or through localization using resting-state network estimates  
415 [45]. However, experience suggests that substantial amount of scan data are required to predict individual  
416 functional data better than the group map. We confirm this by showing that the probabilistic group  
417 map provided by our new atlas is as good as 20 min of individual data (Fig. 5d), rendering individual  
418 localization based on only 10 minutes of data suboptimal. Increasing the individual scan time [15] often  
419 is not feasible, especially in the clinical context.

420 Similarly to the Bayesian model proposed by Kong et al. [16], our new atlas offers an alternative,  
421 by optimally integrating even limited individual data (10-20 minutes) with the probabilistic group map.  
422 This integration yields a probabilistic map of regions in the individual that is better than both group and  
423 individual map.

424 To apply this approach to a new subject in a new study, one needs to acquire some independent  
425 individual localization data (see below). Our framework can then be used to train a new dataset-specific  
426 emission model that characterizes - for each cerebellar region - the average group response on the tasks  
427 contained in that localizer scan. The final individual parcellations are obtained by combining the data  
428 likelihood with the probabilistic group map (see methods: Group and individual parcellations). This  
429 method enables the use of individual functional localization in studies for which the time with each  
430 individual is restricted. Even for longer localizer scans, our approach leads to significant improvement  
431 than using the individual data alone. The code and documentation for individual precision mapping is  
432 available at [github.com/DiedrichsenLab/HierarchBayesParcel](https://github.com/DiedrichsenLab/HierarchBayesParcel).

433 An important consideration for a precision mapping approach remains the decision of whether to use  
434 task-based or resting-state data, and - if using the former - which localizer tasks to include. For many  
435 purposes, it seems advisable to include a set of anchor tasks able to activate each region of interest. We  
436 observed that task-based datasets that focused on a narrow functional domain resulted in precise estimates  
437 of boundaries for regions of that domain at the expense of region boundaries for other domains (Fig. 1a).

438 In addition to tasks that tap into the domain of interest, it is likely beneficial to include tasks that  
439 activate spatially neighboring regions. For example, when aiming to study the language regions of the  
440 cerebellum [31], adding tasks that activate the neighboring multi-demand regions may help to obtain a  
441 more precise estimate of the functional boundary between social-linguistic-spatial and multi-demand  
442 regions, which appear especially variable. The development of a principled approach to design optimal  
443 task-sets for functional localization remains an important question for future research.

444 Overall, functional precision mapping will likely be increasingly important in the future to study the  
445 function of smaller, more variable subregions, study brain connectivity [46, 9], targeted neuromodulation  
446 [47, 48, 49], and individualized diagnostic and prognosis.

## 447 **Lateralization**

448 The cerebellum's importance in lateralized higher-order functions, particularly language, has reignited  
449 interest in lateralization studies of the cerebellum [18]. Studies of hemispheric specialization are most  
450 easily performed using a functional atlas that has regions matched in size and location across hemispheres,  
451 while as closely as possible representing functional boundaries. Prior studies that examined hemispheric  
452 differences in cerebellar development [18] or neurochemistry [50] had to rely on anatomical parcellations,  
453 even though these are not good descriptions of functional subdivisions [3]. Our symmetric atlas addresses  
454 this gap, and we show that the symmetry constraint had only a relatively small impact on its ability to  
455 identify functional subdivisions.

## 456 **Cerebro-cerebellar connectivity**

457 For each of the cerebellar regions, our framework also provides a cerebral connectivity pattern. We  
458 showed that a model that integrates data across diverse task-based dataset outperforms our previous model  
459 that was only trained on the MDTB dataset [28]. These patterns of cerebral connectivity not only provide  
460 an additional description of the identified regions but have two further practical applications.

461 First, being able to identify a cerebellar region by its cerebral pattern of connectivity allows the use of  
462 resting-state data to localize these regions in single individuals [7, 15]. This enables the extension of the  
463 atlas to patient groups and young children and allows users to leverage the broadly available resting-state  
464 datasets.

465 Secondly, the independent identification of the cerebral regions that communicate with each cerebellar  
466 region is an important prerequisite for further studies that investigates the functional differences between  
467 cerebral and cerebellar areas within the same functional module [51]. We therefore believe that the new  
468 atlas will provide an important resource for the study of the human cerebellum going forward.

## 469 **METHODS**

### 470 **Datasets and data organization**

471 We used seven task-based and one resting-state fMRI datasets (see Supplemental Table 1). Each of the  
472 first four datasets comprised a broad battery of tasks tapping into cognitive, motor, perceptual, and social  
473 functions: (1) The *Multi-Domain Task Battery* dataset (MDTB, [3]), (2) a high-resolution version of the  
474 MDTB (*High-res MDTB*; not yet published), (3) the *Nakai & Nishimoto* dataset [52], and the (4) The  
475 *Individual Brain Charting (IBC)* dataset [53, 54]. We also included three further datasets to obtain a  
476 better description of the motor and executive functions: (5) the working memory (*WM*) dataset [51] which  
477 included finger movements and a forward / backwards digit span task; (6) the *Multi-Demand* dataset [26]  
478 which included a no-go, n-back, and task-switch task ; and (7) the *Somatotopic* dataset [22] which probed  
479 foot, hand, glutes, and tongue movements. Finally, we used the resting-state fMRI dataset *Unrelated 100*  
480 subjects, which is made publicly available in the *Human Connectome Project (HCP)* S1200 release [55].

481 The task-based datasets were preprocessed as described in [8]. For each run and condition, we  
482 estimated one contrast image, and divided it by the root-mean-square-error from the first-level GLM  
483 to obtain a normalized activation estimate for each condition. These values served as the input data  
484 for all subsequent analyses. No smoothing or group normalization was applied at this stage. For the  
485 HCP resting-state data, we used minimally preprocessed time series [56]. The preprocessing pipeline  
486 included correction for spatial distortion and head motion, registration to the structural data, cortical  
487 surface mapping, and functional artifact removal [56, 57]. This resulted in 1200 time points of processed  
488 time series per imaging run per cerebellar voxel of the standard MNI152 template [58]. To obtain resting-  
489 state functional connectivity (rs-FC) fingerprints of the cerebellar voxels, we used a group Independent  
490 Component Analysis (ICA). We applied the group-ICA implemented in FSL's MELODIC [59] with  
491 automatic dimensionality estimation to the temporally concatenated functional data of all subjects, sessions  
492 and runs, and selected the top 69 signal components. We then regressed the 69 group network spatial  
493 maps into each subject's data, resulting in 69 subject-specific network time courses. The cerebellar rs-FC  
494 fingerprints were calculated as Pearson's correlations of the cerebellar voxel time series with each cortical  
495 network time course.

496 Using a unified code framework (available at [github.com/diedrichsenlab/Functional\\_](https://github.com/diedrichsenlab/Functional_Fusion)  
497 *Fusion*), the data were then extracted in two atlas spaces. For the cerebellum, we computed the non-  
498 linear morph into the Symmetric MNI152NLin2009aSym template ([http://nist.mni.mcgill.](http://nist.mni.mcgill.ca/?p=904)  
499 *ca/?p=904*). The functional data were resampled to a group space of 18290 cerebellar gray-matter  
500 voxels with an isotropic resolution of 2mm. During this step, we only considered voxels within the  
501 individual cerebellar mask, taking care to exclude any signals from the directly abutting neocortical  
502 regions. For interpolation of functional signals within the cerebellum we used a Gaussian kernel of 2mm  
503 standard deviation. For the cortical-cerebellar connectivity models, the same data were projected onto  
504 individual surfaces, which are aligned to the symmetric freesurfer32LR template [60].

### 505 **Hierarchical Bayesian parcellation framework**

506 To integrate different datasets into a unified probabilistic parcellation atlas, we utilized a newly developed  
507 Hierarchical Bayesian Framework [for full details 8]. In short, the framework integrates different fMRI  
508 datasets,  $\mathbf{Y}^{s,n}$ , recorded in different sessions ( $n$ ) from different subjects ( $s$ ). The model assigns each of the

509 possible brain locations in each individual to one of  $K$  functional parcels, with  $\mathbf{U}_{k,i}^s = 1$  indicating that the  
510  $i^{\text{th}}$  voxel is part of the  $k^{\text{th}}$  parcel. The model estimates the expected value of these parcel assignments,  
511 which provides a probabilistic parcellation for that individual.

512 The model consists of two parts: First, a collection of dataset-specific *emission models* that specify  
513 the probability of each observed dataset given the individual brain parcellation,  $p(\mathbf{Y}^{s,n}|\mathbf{U}^s)$ . Here, we  
514 used a van-Mises-Fisher mixture model, in which each parcel had a mean vector  $\mathbf{v}_k^n$  for each session, and  
515 a separate concentration parameter for each session [ $\kappa^n$ , Model Type 2, see 8]. Each emission model  
516 therefore had the parameters  $\theta_E^n = \{\mathbf{v}_1^n, \dots, \mathbf{v}_k^n, \kappa^n\}$ .

517 The second component, the *arrangement model*, specifies the group probability of each brain location  
518 belonging to a specific parcel. Here we used a model that treated each voxel independently, with  
519  $p(\mathbf{U}_{k,i}^s) = \text{softmax}(\eta_{k,i})$ . The  $K \times P$  arrangement model parameters  $\theta_A = \{\eta_{1,1}, \dots\}$  could therefore be  
520 estimated by averaging across all the individual probability maps. During this integration step, the  
521 concentration parameter for each dataset effectively determines the weight by which an individual  
522 contributes to the overall group map.

523 The parameters of the spatial arrangement models and the emission models were estimated together  
524 using an EM-algorithm. We used 5000 different random starting values to avoid local minima. For  
525 computational reasons, the initial fitting and evaluation was done using a 3mm isotropic voxel resolution -  
526 the final selected model was upsampled to 2mm and used as a starting value to refit to the higher resolution  
527 data.

### 528 **Symmetry constraint**

529 To achieve spatially symmetric parcellations, we developed a version of the arrangement model, where  
530 parcels  $1 \dots K/2$  were restricted to the left hemisphere, and parcel  $K/2 + 1, \dots, K$  to the right. The  
531 assignment of voxels to parcels was symmetric - that is if the left hemisphere voxel was assigned to  
532 parcel 1, the corresponding right hemispheric voxel was assigned to parcel  $K/2 + 1$ . As a consequence,  
533 symmetric brain locations were assigned to corresponding parcels. The mean functional profiles  $\mathbf{v}_k^n$ ,  
534 however, were estimated separately for the left and right hemispheric parcels. This allowed us to derive a  
535 spatially symmetric parcellation of the cerebellum, while still capturing the functional specialization of  
536 each hemisphere.

537 To construct a corresponding asymmetric atlas, we removed the symmetry constraint, now allowing  
538 left and right-hemispheric voxels to be assigned to non-matching parcels. However, to retain the same  
539 number of regions, we retained the constraint that one half of the regions were in the left, the other half  
540 in the right hemisphere. To make the asymmetric atlas comparable to the symmetric version, we also  
541 used the fitted emission models (mean functional profiles) from the symmetric model, only refitting the  
542 arrangement model without the symmetry constraint. This resulted in an asymmetric version of the atlas  
543 in which the regions had the same functional profiles as in the symmetric version.

### 544 **Group and individual parcellations**

545 After fitting the parameters  $\{\theta_A, \theta_E^1, \dots, \theta_E^N\}$ , the model can be used to derive both a group and individual  
546 parcellation maps. The probabilistic group parcellation is based only on the arrangement model, which  
547 directly specifies  $p_{\text{group}} = p(\mathbf{U})$  for each voxel and parcel. Each individual parcellation is based on some  
548 *individual training data*,  $\mathbf{Y}_s^n$ . The data-only parcellation only depends on the corresponding emission  
549 model, with  $p_{\text{data},s} \propto p(\mathbf{Y}_s^n|\mathbf{U}_s)$ . In contrast, the full individual parcellation integrates the probability from  
550 both emission and arrangement model  $p_{\text{div},s} \propto p(\mathbf{Y}_s^n|\mathbf{U}_s)p(\mathbf{U}_s)$ , using Bayes rule. For visualization and  
551 evaluation, both group and individual probabilistic parcellation were transformed into hard parcellations  
552 by assigning each voxel the parcel with the highest probability.

### 553 **Individual precision mapping**

554 Our model provides a probabilistic group map (spatial arrangement model) and a probabilistic estimate of  
555 parcel membership based on a specific individual data set (using a dataset-specific emission model). By  
556 integrating these using Bayes rule, an optimal estimate of brain organization for a new individual can  
557 be obtained [8]. For the analysis presented in Fig. 5, we used 1-16 runs of data from the first task set of  
558 the MDTB dataset as training. The individual maps were then evaluated on the second task set, which  
559 contained 8 overlapping and 9 novel tasks [3].

560 To apply this approach to new subjects with individual localizing data that is different from the  
561 task sets included in our atlas, the user would first estimate a new emission model from the data of all

562 individuals in the study. This new dataset-specific emission model can be used to localize regions in new  
563 individuals, given their data.

#### 564 **Single-dataset parcellations and similarity analysis of parcellations**

565 To compare the differences between parcellations derived from different datasets, we trained the model on  
566 each dataset separately, estimating parcellation maps with 10, 20, 34, 40 and 68 regions. As an index of  
567 parcellation similarity, we calculated the adjusted Rand Index (ARI) between the winner-take-all voxel  
568 assignments of the resulting parcellations. The ARI was calculated across all 5 levels of granularity,  
569 resulting in a 5x5 matrix of ARIs for each dataset pair. Different datasets are differently reliable which  
570 could affect the similarity of two datasets. We therefore estimated the reliability of the parcellation by  
571 averaging the ARIs between different levels of granularity within each dataset, with the idea that reliable  
572 datasets should result in parcellations that are consistent across granularities. We then divided the ARI  
573 (also average across levels of granularity) between two datasets by the geometric mean of the two average  
574 within-dataset ARIs. This index served as a reliability corrected measure of correspondence between  
575 parcellations.

576 Statistical tests to compare the similarity of two data set pairs were performed using a paired t-test,  
577 using reliability-corrected ARIs for the unique 25 different granularity pairs as independent observations.

578 Finally, we used classic multi-dimensional scaling to visualize the structure of similarities between  
579 different parcellations. We calculated the first two eigenvectors of the square matrix of adjusted between-  
580 dataset similarities. The space defined by these two vectors optimally reproduces the overall similarity  
581 structure, with the dissimilarity (1-ARI) between two datasets reflected in the Euclidean distance between  
582 the two.

#### 583 **DCBC evaluation**

584 To assess how well a given parcellation can predict functional boundaries in the cerebellum, we utilized the  
585 Distance-Controlled Boundary Coefficient (DCBC) [23]. This metric compares the correlation between  
586 voxel-pairs within a parcel to the correlation between voxel-pairs across a boundary, while accounting  
587 for spatial distance. Our evaluation included both the group parcellation (DCBC group) and individual  
588 parcellations (DCBC individual) obtained from this group atlas.

589 Both group and individual DCBC were calculated in a cross-validated fashion, leaving out the test  
590 dataset during training of the overall model. The group DCBC was calculated by deriving a winner-take-all  
591 parcellation from the group probability map and evaluating the ability of these group-based boundaries to  
592 predict functional boundaries in each individual.

593 To calculate the DCBC for individual parcellations, we used a localizer-like approach for individual  
594 precision mapping (see methods: individual precision mapping): One half of the test dataset served  
595 as the localizer data. First, we estimated a dataset-specific emission model for the localizer dataset  
596 across all subjects. Then, we used the localizer data from one specific subject to estimate the individual  
597 boundaries (see methods: group and individual parcellations). Hard-parcellated individual boundaries  
598 were derived using a winner-take-all approach on the subject's resultant individual probability map. These  
599 were then tested for their ability to predict functional boundaries in the second half of the subject's data.  
600 We then reversed the role of the two halves of the test set averaged performance across the two within-  
601 subject cross-validation folds. To make the evaluation of group-based and individual-based boundaries  
602 comparable, we also calculated the group DCBC by splitting each subject's data in half and then averaging  
603 the performance across the two halves after individual DCBC calculation. A higher DCBC value indicates  
604 better performance of the parcellation.

#### 605 **Prediction error evaluation**

606 To assess the ability of a given parcellation to predict functional responses in individual held-out data,  
607 we calculated a prediction error. Using the same localizer-like approach as for the individual DCBC, we  
608 first derived the individual parcellations from one half of each dataset, and converted these to winner-take  
609 all maps. We then used the data from  $N - 1$  subjects of the second half to estimate the mean functional  
610 profiles ( $\mathbf{v}_k$ ) for each region. For each voxel in the  $N^{th}$  subject, we then used the profile of the assigned  
611 region as a prediction and calculated the prediction error as one minus the cosine similarity of prediction  
612 and data vector. When averaging these results across voxels, we weighted each cosine error by the length  
613 of the data vector to ensure that voxels with high signal strength would influence our evaluation more  
614 than noisy voxels [8].

## 615 **Parcel similarity and clustering**

616 To develop a hierarchically organized system of maps, we started with the symmetric map with 68 parcels  
617 (34 per hemisphere) as our base. For clustering we derived a functional similarity index between parcels.  
618 We first averaged the estimated mean response vectors for each parcel and session  $\mathbf{v}_k^n$  across the left and  
619 right hemisphere, and then calculated the cosine similarity between each pair of parcels. We then took the  
620 weighted average of these cosine-similarities across sessions and datasets, with the weight of each session  
621 set to product of the dispersion parameter  $\kappa^n$  and number of subjects for that session  $N^n$ .

622 We then iteratively merged the smallest parcels into the functionally most similar parcel, until  
623 all parcels had at least one voxel win the winner-take-all assignment, resulting in 32 parcels (16 per  
624 hemisphere). When merging parcels, we summed their probability maps to obtain the probability of a  
625 voxel to belong to the combined parcel. The emission models for the combined model were then refit  
626 to the data, keeping the probabilities in the arrangement model fixed. In a last step, we grouped the 32  
627 parcels (again, based on their functional profiles) into 4 domains. The labels for each parcel then followed  
628 the organization of Domain-Region-Hemisphere-Subregion.

629 The colormap for our functional atlas was based on the weighted cosine similarity of the functional  
630 profiles (see above). We used classical multi-dimensional-scaling to represent these similarities in a  
631 3-dimensional space. This arrangement was then projected into RGB space. We used 3 spatial anchor  
632 points (motor region = green, demand = red, social linguistic = yellow) to achieve a consistent color  
633 scheme across parcellations (i.e. Figure 1a). As a result, the similarity of color of different parcels can be  
634 directly interpreted as an approximation of their functional similarity.

## 635 **Functional lateralization and Boundary symmetry**

636 To study lateralization, we assessed the symmetry of the functional profiles of left-right voxel pairs. For  
637 this, we calculated the cosine similarity of the functional profiles of each voxel pair. Functional profiles  
638 were obtained by averaging the estimated mean response vectors for each voxel in each session. The  
639 cosine similarities were then weighted by the session weight  $\kappa^n$  and the number of subjects  $N^n$ , for session  
640  $n$ .

641 To investigate left-right boundary symmetry in the cerebellum, an asymmetric version of the atlas  
642 was estimated (see methods: Symmetry constraint). An index of boundary symmetry was calculated  
643 as the correlation between the parcel probability vectors of the asymmetric and the symmetric atlas for  
644 each voxel, either for the group map, or for the individual parcellations. For visualization, the correlation  
645 values within all datasets, excluding the Nishimoto and IBC dataset due to the relatively low reliabilities,  
646 were averaged across individuals.

## 647 **Cerebral cortical connectivity**

648 Connectivity models were fitted for each individual (and dataset) separately. As described in King et al.  
649 [28], we parcellated the cerebral cortex into 1876 parcels using a regular icosahedron. For task-based  
650 data we used the normalized activity estimates, for the resting-state data, the preprocessed time series  
651 (see methods: Datasets and data organization). These data were averaged across all voxels in each  
652 cerebral ROI, forming the  $N \times Q$  matrix  $\mathbf{X}$ . The same data was extracted for each cerebellar voxel in atlas  
653 space. The connectivity weights were then estimated to form the best predictive model  $\mathbf{Y} = \mathbf{X}\mathbf{W}$  using  
654 Ridge-regression. The ridge coefficient was tuned for each dataset separately to yield the best prediction  
655 performance on all the other datasets.

656 For evaluation, we averaged the connectivity weight across all subjects in each training dataset. For  
657 each individual in the evaluation dataset, we used the cerebral cortical activity measures and the average  
658 connectivity weights to predict the individual cerebellar activity patterns. We then calculated the cosine  
659 similarity between the predicted and observed cerebellar activity [28].

660 When evaluating a connectivity model on the same dataset it was trained on, we adopted a leave-  
661 one-subject out approach. For each individual, the connectivity weights were averaged across all other  
662 individuals in that dataset, and then applied to make the prediction for that single subject.

663 Finally, we investigated if an integration across all datasets would increase the predictive power of  
664 the connectivity model. For this we simply averaged connectivity models across all task-based datasets,  
665 always taking care to leave the particular evaluation subject out of the averaging of the connectivity  
666 weights.

667 **Functional profiles for the MDTB dataset**

668 To characterize the functional profile of each cerebellar region, we calculated the mean task response  
669 of all parcels in the MDTB dataset. These functional profiles were the normalized activation estimates  
670 (see methods: Dataset and Data Organization), averaged across the individualized regions within each  
671 individual. To account for activation that can be explained by the motor aspects of each task, we used the  
672 number of movements in each condition (left hand presses, right hand presses and saccades per second) as  
673 a covariate alongside regressors that coded for each condition separately [3]. The columns of the design  
674 matrix and the average functional profiles were z-normalized across conditions. We estimated a linear  
675 model using ridge regression (L2 regularization) to arrive at a final estimate for the motor features and  
676 task-activations.

677 **Inter-individual variability**

678 To quantify inter-individual variability in the cerebellum, we calculated Pearson's correlation coefficient  
679 of each voxel's response profile pairwise between all subjects within the MDTB dataset. To account for  
680 the measurement noise, we derived two independent estimates for each subject and voxel: one from the  
681 first half, the other from the second half of the data. Correlations were computed on the concatenated two  
682 profiles and the reliability was calculated by correlating the two independent estimates of the response  
683 profile within each subject. The inter-subject correlation was normalized by dividing each value by the  
684 square root of the product of the two subject's reliabilities. For purposes of visualization of each voxel's  
685 inter-individual variability, we averaged the inter-subject correlation values across subjects and divided it  
686 by the reliability averaged across subjects, obtaining a single value per voxel. These voxel values were  
687 projected to the flatmap.

## REFERENCES

- 688
- 689 [1] Peter L Strick, Richard P Dum, and Julie A Fiez. Cerebellum and nonmotor function. *Annu. Rev. Neurosci.*, 32:413–434, 2009.
- 690
- 691 [2] Jeremy D Schmahmann. Disorders of the cerebellum: Ataxia, dysmetria of thought, and the cerebellar cognitive affective syndrome. *J. Nurse Pract.*, 16(3):367–378, August 2004.
- 692
- 693 [3] Maedbh King, Carlos R Hernandez-Castillo, Russell A Poldrack, Richard B Ivry, and Jörn Diedrichsen. Functional boundaries in the human cerebellum revealed by a multi-domain task battery. *Nature neuroscience*, 22(8):1371–1378, 2019.
- 694
- 695 [4] J D Schmahmann, J Doyon, D McDonald, C Holmes, K Lavoie, A S Hurwitz, N Kabani, A Toga, A Evans, and M Petrides. Three-dimensional MRI atlas of the human cerebellum in proportional stereotaxic space. *Neuroimage*, 10(3 Pt 1):233–260, 1999.
- 696
- 697 [5] J Diedrichsen, J H H Balsters, J Flavell, E Cussans, and N Ramnani. A probabilistic MR atlas of the human cerebellum. *Neuroimage*, 46(1):39–46, 2009.
- 698
- 699 [6] Jie Lisa Ji, Marjolein Spronk, Kaustubh Kulkarni, Grega Repovš, Alan Anticevic, and Michael W Cole. Mapping the human brain’s cortical-subcortical functional network organization. *Neuroimage*, 185:35–57, 2019.
- 700
- 701 [7] Randy L Buckner, Fenna M Krienen, Angela Castellanos, Julio C Diaz, and BT Thomas Yeo. The organization of the human cerebellum estimated by intrinsic functional connectivity. *Journal of neurophysiology*, 106(5):2322–2345, 2011.
- 702
- 703 [8] Da Zhi, Ladan Shahshahani, Caroline Nettekoven, Ana Luisa Pinho, Danilo Bzdok, and Joern Diedrichsen. A hierarchical bayesian brain parcellation framework for fusion of functional imaging datasets. *bioRxiv*, 2023.
- 704
- 705 [9] Janine Bijsterbosch, Samuel J Harrison, Saad Jbabdi, Mark Woolrich, Christian Beckmann, Stephen Smith, and Eugene P Duff. Challenges and future directions for representations of functional brain organization. *Nature neuroscience*, 23(12):1484–1495, 2020.
- 706
- 707 [10] Timothy O Laumann, Evan M Gordon, Babatunde Adeyemo, Abraham Z Snyder, Sung Jun Joo, Mei-Yen Chen, Adrian W Gilmore, Kathleen B McDermott, Steven M Nelson, Nico UF Dosenbach, et al. Functional system and areal organization of a highly sampled individual human brain. *Neuron*, 87(3):657–670, 2015.
- 708
- 709 [11] Rodrigo M Braga and Randy L Buckner. Parallel interdigitated distributed networks within the individual estimated by intrinsic functional connectivity. *Neuron*, 95(2):457–471, 2017.
- 710
- 711 [12] Evan M Gordon, Timothy O Laumann, Babatunde Adeyemo, Adrian W Gilmore, Steven M Nelson, Nico UF Dosenbach, and Steven E Petersen. Individual-specific features of brain systems identified with resting state functional correlations. *Neuroimage*, 146:918–939, 2017.
- 712
- 713 [13] Sophia Mueller, Danhong Wang, Michael D Fox, BT Thomas Yeo, Jorge Sepulcre, Mert R Sabuncu, Rebecca Shafee, Jie Lu, and Hesheng Liu. Individual variability in functional connectivity architecture of the human brain. *Neuron*, 77(3):586–595, 2013.
- 714
- 715 [14] Scott Marek, Joshua S Siegel, Evan M Gordon, Ryan V Raut, Caterina Gratton, Dillan J Newbold, Mario Ortega, Timothy O Laumann, Babatunde Adeyemo, Derek B Miller, et al. Spatial and temporal organization of the individual human cerebellum. *Neuron*, 100(4):977–993, 2018.
- 716
- 717 [15] Aihuiping Xue, Ru Kong, Qing Yang, Mark C. Eldaief, Peter Angeli, Lauren M DiNicola, Rodrigo M. Braga, Randy L Buckner, and B.T. Thomas Yeo. The Detailed Organization of the Human Cerebellum Estimated by Intrinsic Functional Connectivity Within the Individual. *J. Neurophysiol.*, 1(September 2020):358–384, 2020.
- 718
- 719 [16] Ru Kong, Jingwei Li, Csaba Orban, Mert R Sabuncu, Hesheng Liu, Alexander Schaefer, Nanbo Sun, Xi-Nian Zuo, Avram J Holmes, Simon B Eickhoff, et al. Spatial topography of individual-specific cortical networks predicts human cognition, personality, and emotion. *Cerebral cortex*, 29(6):2533–2551, 2019.
- 720
- 721 [17] S. E. Petersen, P. T. Fox, M. I. Posner, M. Mintun, and M. E. Raichle. Positron emission tomographic studies of the processing of single words. *Journal of Cognitive Neuroscience*, 1(2):153–170, 1989.
- 722
- 723 [18] Carolin Gaiser, Rick van der Vliet, Augustijn de Boer, Opher Donchin, Pierre Berthet, Gabriel Devenyi, Mallar Chakravarty, Jörn Diedrichsen, Andre Marquand, Maarten Frens, and Ryan Muetzel. Large data on the small brain: Population-wide cerebellar growth models of children and adolescents, 2023.
- 724
- 725 [19] Jörn Diedrichsen and Ewa Zotow. Surface-based display of volume-averaged cerebellar imaging data.
- 726
- 727
- 728
- 729
- 730
- 731
- 732
- 733
- 734
- 735
- 736
- 737
- 738
- 739
- 740
- 741
- 742

- 743 *PloS one*, 10(7):e0133402, 2015.
- 744 [20] Michael W Cole, Danielle S Bassett, Jonathan D Power, Todd S Braver, and Steven E Petersen.  
745 Intrinsic and task-evoked network architectures of the human brain. *Neuron*, 83(1):238–251, 2014.
- 746 [21] I Tavor, O Parker Jones, R B Mars, S M Smith, T E Behrens, and S Jbabdi. Task-free MRI predicts  
747 individual differences in brain activity during task performance. *Science*, 352(6282):216–220, 2016.
- 748 [22] Noam Saadon-Grosman, Peter A Angeli, Lauren M DiNicola, and Randy L Buckner. A third  
749 somatomotor representation in the human cerebellum. *Journal of Neurophysiology*, 128(4):1051–  
750 1073, 2022.
- 751 [23] Da Zhi, Maedbh King, Carlos R Hernandez-Castillo, and Jörn Diedrichsen. Evaluating brain  
752 parcellations using the distance-controlled boundary coefficient. *Human Brain Mapping*, 43(12):3706–  
753 3720, 2022.
- 754 [24] Daniel Marten van Es, Wietske van der Zwaag, and Tomas Knapen. Retinotopic maps of visual space  
755 in the human cerebellum. *Current Biology*, 1 2019.
- 756 [25] John Duncan, Moataz Assem, and Sneha Shashidhara. Integrated intelligence from distributed brain  
757 activity. *Trends in cognitive sciences*, 24:838–852, 10 2020.
- 758 [26] Moataz Assem, Sneha Shashidhara, Matthew F Glasser, and John Duncan. Basis of executive  
759 functions in fine-grained architecture of cortical and subcortical human brain networks. *bioRxiv*,  
760 2022.
- 761 [27] Lauren M. DiNicola, Rodrigo M. Braga, and Randy L. Buckner. Parallel distributed networks disso-  
762 ciate episodic and social functions within the individual. *Journal of Neurophysiology*, 123(3):1144–  
763 1179, 2020.
- 764 [28] Maedbh King, Ladan Shahshahani, Richard B Ivry, and Jörn Diedrichsen. A task-general connectivity  
765 model reveals variation in convergence of cortical inputs to functional regions of the cerebellum.  
766 *eLife*, 12, 4 2023.
- 767 [29] Jingnan Du, Lauren M Dinicola, Peter A Angeli, Noam Saadon-grosman, Wendy Sun, Stephanie  
768 Kaiser, Joanna Ladopoulou, Aihuiping Xue, B T Thomas Yeo, Mark C Eldaief, and Randy L Buckner.  
769 Within-Individual Organization of the Human Cerebral Cortex : Networks , Global Topography , and  
770 Function. *bioRxiv*, pages 1–88, 2023.
- 771 [30] Rebecca Saxe, Matthew Brett, and Nancy Kanwisher. Divide and Conquer: A Defense of Functional  
772 Localizers. *Neuroimage*, 04 2010.
- 773 [31] Evelina Fedorenko, Po Jang Hsieh, Alfonso Nieto-Castañón, Susan Whitfield-Gabrieli, and Nancy  
774 Kanwisher. New method for fMRI investigations of language: Defining ROIs functionally in  
775 individual subjects. *Journal of Neurophysiology*, 2010.
- 776 [32] David Dodell-Feder, Jorie Koster-Hale, Marina Bedny, and Rebecca Saxe. fmri item analysis in a  
777 theory of mind task. *NeuroImage*, 55(2):705–712, 2011.
- 778 [33] Xavier Guell, Jeremy D Schmahmann, John DE Gabrieli, and Satrajit S Ghosh. Functional gradients  
779 of the cerebellum. *Elife*, 7:e36652, 2018.
- 780 [34] Martin I. Sereno, J. rn Diedrichsen, Mohamed Tachrount, Guilherme Testa-Silva, Helen D Arceuil,  
781 and Chris De Zeeuw. The human cerebellum has almost 80neocortex. *Proceedings of the National*  
782 *Academy of Sciences of the United States of America*, 117(32):19538–19543, 2020.
- 783 [35] Catherine J. Stoodley, Jason P. MacMore, Nikos Makris, Janet C. Sherman, and Jeremy D. Schmah-  
784 mann. Location of lesion determines motor vs. cognitive consequences in patients with cerebellar  
785 stroke. *NeuroImage: Clinical*, 12:765–775, 2016.
- 786 [36] Renée F. Schild. On the inferior olive of the albino rat. *Journal of Comparative Neurology*, 1970.
- 787 [37] I. Sugihara, H. S. Wu, and Y. Shinoda. The entire trajectories of single olivocerebellar axons in the  
788 cerebellar cortex and their contribution to cerebellar compartmentalization. *Journal of Neuroscience*,  
789 2001.
- 790 [38] Mohammad Shahangir Biswas, Yuanjun Luo, Gideon Anokye Sarpong, and Izumi Sugihara. Diver-  
791 gent projections of single pontocerebellar axons to multiple cerebellar lobules in the mouse. *Journal*  
792 *of Comparative Neurology*, 527(12):1966–1985, 2019.
- 793 [39] Scott Marek, Joshua S. Siegel, Evan M. Gordon, Ryan V. Raut, Caterina Gratton, Dillan J. Newbold,  
794 Mario Ortega, Timothy O. Laumann, Babatunde Adeyemo, Derek B. Miller, Annie Zheng, Kather-  
795 ine C. Lopez, Jeffrey J. Berg, Rebecca S. Coalson, Annie L. Nguyen, Donna Dierker, Andrew N.  
796 Van, Catherine R. Hoyt, Kathleen B. McDermott, Scott A. Norris, Joshua S. Shimony, Abraham Z.  
797 Snyder, Steven M. Nelson, Deanna M. Barch, Bradley L. Schlaggar, Marcus E. Raichle, Steven E.



- 798 Petersen, Deanna J. Greene, and Nico U.F. Dosenbach. Spatial and Temporal Organization of the  
799 Individual Human Cerebellum. *Neuron*, 100(4):977–993.e7, 2018.
- 800 [40] Kyle Mahowald and Evelina Fedorenko. Reliable individual-level neural markers of high-level  
801 language processing: A necessary precursor for relating neural variability to behavioral and genetic  
802 variability. *NeuroImage*, 139:74–93, 2016.
- 803 [41] Evelina Fedorenko, Anna A Ivanova, and Tamar I Regev. The language network as a natural kind  
804 within the broader landscape of the human brain. *Nature Reviews Neuroscience*, 2024.
- 805 [42] Frank Van Overwalle, Min Pu, Qianying Ma, Meijia Li, Naem Haihambo, Kris Baetens, Natacha  
806 Deroost, Chris Baeken, and Elien Heleven. The Involvement of the Posterior Cerebellum in Recon-  
807 structing and Predicting Social Action Sequences. *Cerebellum*, 21(5):733–741, 2022.
- 808 [43] Anila M. D’Mello, Peter E. Turkeltaub, and Catherine J. Stoodley. Cerebellar tDCS modulates  
809 neural circuits during semantic prediction: A combined tDCS-fMRI study. *Journal of Neuroscience*,  
810 37(6):1604–1613, 2017.
- 811 [44] Anila M. D’Mello, John D.E. Gabrieli, and Derek Evan Nee. Evidence for Hierarchical Cognitive  
812 Control in the Human Cerebellum. *Current Biology*, 30(10):1881–1892.e3, 2020.
- 813 [45] Rodrigo M. Braga, Lauren M. DiNicola, Hannah C. Becker, and Randy L. Buckner. Situating the  
814 left-lateralized language network in the broader organization of multiple specialized large-scale  
815 distributed networks. *Journal of Neurophysiology*, 124(5):1415–1448, 2020. PMID: 32965153.
- 816 [46] Janine Diane Bijsterbosch, Mark W. Woolrich, Matthew F. Glasser, Emma C. Robinson, Christian F.  
817 Beckmann, David C. Van Essen, Samuel J. Harrison, and Stephen M. Smith. The relationship  
818 between spatial configuration and functional connectivity of brain regions. *eLife*, 7, 2 2018.
- 819 [47] Michael D. Fox, Randy L. Buckner, Matthew P. White, Michael D. Greicius, and Alvaro Pascual-  
820 Leone. Efficacy of transcranial magnetic stimulation targets for depression is related to intrinsic  
821 functional connectivity with the subgenual cingulate. *Biological Psychiatry*, 72(7):595–603, 2012.
- 822 [48] Robin F.H. Cash, Luca Cocchi, Jinglei Lv, Paul B. Fitzgerald, and Andrew Zalesky. Functional Mag-  
823 netic Resonance Imaging-Guided Personalization of Transcranial Magnetic Stimulation Treatment  
824 for Depression. *JAMA Psychiatry*, 78(3):337–339, 2021.
- 825 [49] Robin F.H. Cash, Andrew Zalesky, Richard H. Thomson, Ye Tian, Luca Cocchi, and Paul B. Fitzgerald.  
826 Subgenual Functional Connectivity Predicts Antidepressant Treatment Response to Transcranial  
827 Magnetic Stimulation: Independent Validation and Evaluation of Personalization, 2019.
- 828 [50] Caroline Nettekoven, Leah Mitchell, William T. Clarke, Uzay Emir, Jon Campbell, Heidi Johansen-  
829 Berg, Ned Jenkinson, and Charlotte Stagg. Cerebellar GABA Change during Visuomotor Adaptation  
830 Relates to Adaptation Performance and Cerebellar Network Connectivity: A Magnetic Resonance  
831 Spectroscopic Imaging Study. *The Journal of Neuroscience*, 42(41):JN–RM–0096–22, sep 2022.
- 832 [51] Ladan Shahshahani, Maedbh King, Caroline Nettekoven, Richard Ivry, and Jörn Diedrichsen. Se-  
833 lective recruitment: Evidence for task-dependent gating of inputs to the cerebellum. *bioRxiv*, pages  
834 2023–01, 2023.
- 835 [52] Tomoya Nakai and Shinji Nishimoto. Quantitative models reveal the organization of diverse cognitive  
836 functions in the brain. *Nature communications*, 11(1):1–12, 2020.
- 837 [53] Ana Luísa Pinho, Alexis Amadon, Torsten Ruest, Murielle Fabre, Elvis Dohmatob, Isabelle DENGHIEN,  
838 Chantal Ginisty, Séverine Becuwe-Desmidt, Séverine Roger, Laurence Laurier, et al. Individual brain  
839 charting, a high-resolution fmri dataset for cognitive mapping. *Scientific data*, 5(1):1–15, 2018.
- 840 [54] Ana Luísa Pinho, Alexis Amadon, Baptiste Gauthier, Nicolas Clairis, André Knops, Sarah Genon,  
841 Elvis Dohmatob, Juan Jesús Torre, Chantal Ginisty, Séverine Becuwe-Desmidt, et al. Individual  
842 brain charting dataset extension, second release of high-resolution fmri data for cognitive mapping.  
843 *Scientific Data*, 7(1):353, 2020.
- 844 [55] David C Van Essen, Stephen M Smith, Deanna M Barch, Timothy EJ Behrens, Essa Yacoub, Kamil  
845 Ugurbil, Wu-Minn HCP Consortium, et al. The wu-minn human connectome project: an overview.  
846 *Neuroimage*, 80:62–79, 2013.
- 847 [56] Matthew F. Glasser, Stamatios N. Sotiropoulos, J. Anthony Wilson, Timothy S. Coalson, Bruce Fischl,  
848 Jesper L. Andersson, Junqian Xu, Saad Jbabdi, Matthew Webster, Jonathan R. Polimeni, David C.  
849 Van Essen, and Mark Jenkinson. The minimal preprocessing pipelines for the human connectome  
850 project. *NeuroImage*, 80:105–124, 2013.
- 851 [57] Stephen M Smith, Christian F Beckmann, Jesper Andersson, Edward J Auerbach, Janine Bijsterbosch,  
852 Gwenaëlle Douaud, Eugene Duff, David A Feinberg, Ludovica Griffanti, Michael P Harms, et al.

- 853 Resting-state fmri in the human connectome project. *Neuroimage*, 80:144–168, 2013.
- 854 [58] David C Van Essen, Matthew F Glasser, Donna L Dierker, John Harwell, and Timothy Coalson.  
855 Parcellations and hemispheric asymmetries of human cerebral cortex analyzed on surface-based  
856 atlases. *Cerebral cortex*, 22(10):2241–2262, 2012.
- 857 [59] Mark Jenkinson, Christian F Beckmann, Timothy EJ Behrens, Mark W Woolrich, and Stephen M  
858 Smith. Fsl. *Neuroimage*, 62(2):782–790, 2012.
- 859 [60] David C. Van Essen, Matthew F. Glasser, Donna L. Dierker, John Harwell, and Timothy Coalson.  
860 Parcellations and hemispheric asymmetries of human cerebral cortex analyzed on surface-based  
861 atlases. *Cerebral cortex (New York, N.Y. : 1991)*, 22:2241–2262, 10 2012.

## 862 1 DATA AVAILABILITY

863 The raw data for the fMRI studies used in this project are publicly available on <https://openneuro.org/>  
864 for the MDTB dataset, the Nishimoto dataset and the IBC dataset. For the HCP dataset, raw and pre-  
865 processed data is available at [https://www.humanconnectome.org/study/hcp-young-adult/  
866 data-releases](https://www.humanconnectome.org/study/hcp-young-adult/data-releases). The MDTB-Highres, WMFS and Somatotopic dataset has not yet been openly re-  
867 leased.

## 868 2 CODE AVAILABILITY

869 For a practical example on how to generate individual cerebellar parcellations using a new dataset, see  
870 [https://hierarchbayesparcel.readthedocs.io/en/latest/indiv\\_parcel.html](https://hierarchbayesparcel.readthedocs.io/en/latest/indiv_parcel.html)  
871 The code for the hierarchical Bayesian parcellation framework is available at [https://github.  
872 com/DiedrichsenLab/HierarchBayesParcel](https://github.com/DiedrichsenLab/HierarchBayesParcel). The organization, file system, and code for  
873 managing the diverse set of datasets is available at [https://github.com/DiedrichsenLab/  
874 Functional\\_Fusion](https://github.com/DiedrichsenLab/Functional_Fusion). The code for building the atlas and generating the results and figures in this pa-  
875 per is publicly available as the GitHub repository [https://github.com/DiedrichsenLab/  
876 ProbabilisticParcellation](https://github.com/DiedrichsenLab/ProbabilisticParcellation). The code for connectivity modelling is available at [https:  
877 //github.com/DiedrichsenLab/cortico\\_cereb\\_connectivity](https://github.com/DiedrichsenLab/cortico_cereb_connectivity). For a tutorial on how  
878 to apply the connectivity model to new data to make predictions, see [https://github.com/  
879 DiedrichsenLab/cortico\\_cereb\\_connectivity/blob/main/notebooks/0.Application\\_  
880 example.ipynb](https://github.com/DiedrichsenLab/cortico_cereb_connectivity/blob/main/notebooks/0.Application_example.ipynb)

## 881 ACKNOWLEDGEMENTS

882 This study was supported by a Discovery Grant from the Natural Sciences and Engineering Research  
883 Council of Canada (NSERC, RGPIN-2016-04890), and a project grant from the Canadian Institutes  
884 of Health Research (CIHR, PJT 159520), both to J.D. Additional funding came from the Canada First  
885 Research Excellence Fund (BrainsCAN) to Western University and a National Institute of Mental Health  
886 (MH124004) to R.L.B.. We would like to acknowledge Suzanne Witt for help in collecting and prepro-  
887 cessing the MDTB-Highres dataset. Special thanks to M. Assem, and J. Duncan for sharing their datasets  
888 before the official public release.

## 889 COMPETING INTERESTS

890 The authors declare no competing interests.

891 **SUPPLEMENTARY MATERIALS AND FIGURES**

Name	Subjects	No. conditions	min/subject	Voxel size (mm)	Description
MDTB	24	62	320	3T, 3mm	Cognitive, motor, perceptual, social
Highres-MDTB	8	9	120	7T, 1.5mm	Cognitive, motor, perceptual, social
Nishimoto	6	103	162	3T, 2mm	Cognitive, motor, perceptual, social
IBC	12	208	822	3T, 1.5mm	Cognitive, motor, perceptual, social
WM	16	17	65	3T, 3mm	Motor and working memory task
Multi-demand	37	12	100	3T, 2mm	Executive Tasks
Somatotopic	8	6	96	1.8/2.4	Motor
HCP-Unrelated 100	100	none	60	3T, 2mm	Resting-state

**Table 1. FMRI datasets used for the functional fusion.** All datasets but the last are task-based. The last one refers to resting-state data from a subset of the HCP dataset.

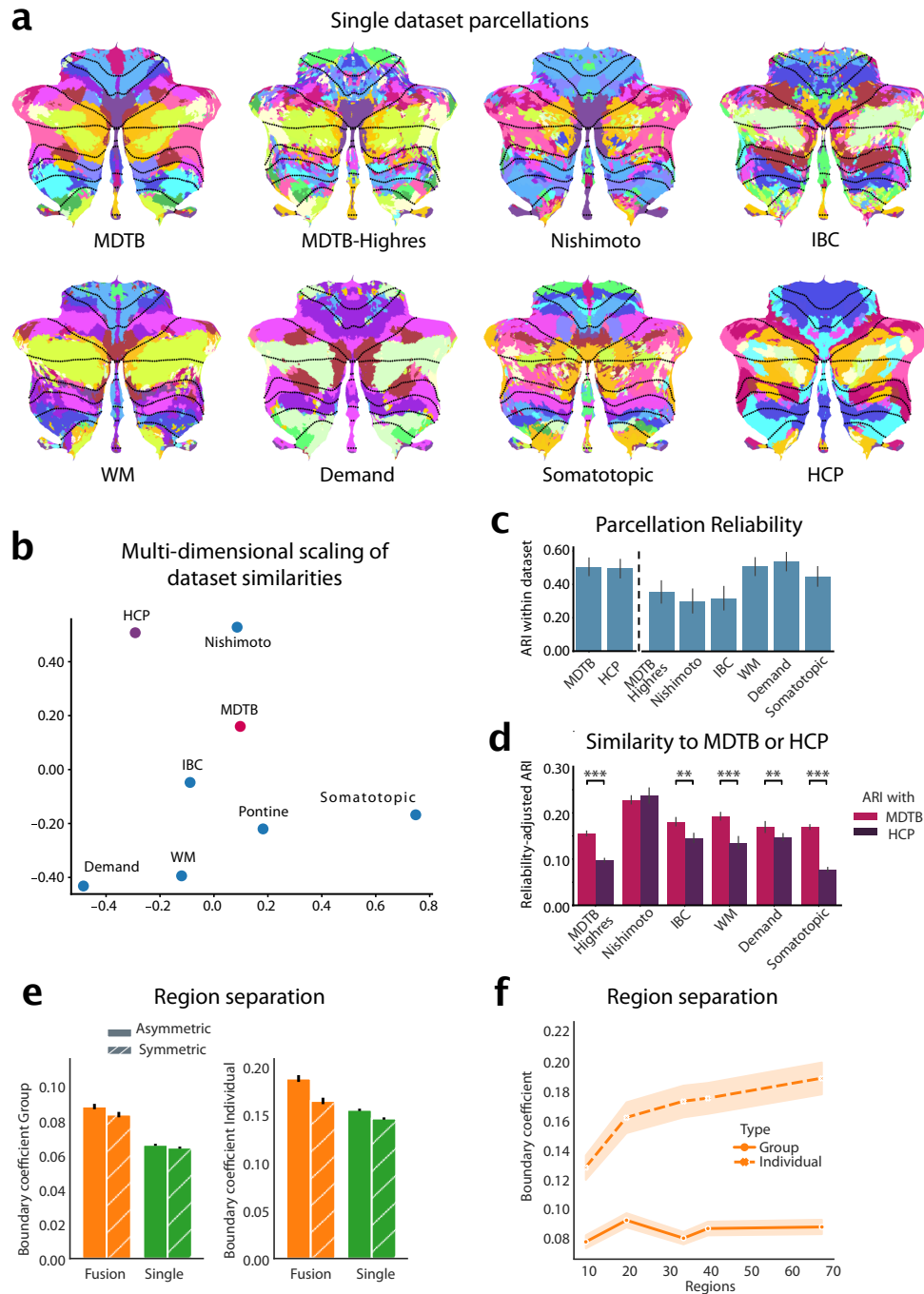


**Figure 1. Building a functional atlas of the cerebellum across datasets.** **a**, Parcellations ( $K=68$ ) derived from each single dataset. The probabilistic parcellation is shown as a winner-take-all projection onto a flattened representation of the cerebellum [19]. Functionally similar regions are colored similarly within a parcellation (see methods: parcel similarity) and spatially similar parcels are assigned similar colors across parcellations. Dotted lines indicate lobular boundaries. **b**, Projection of the between-dataset adjusted Rand Index (ARI) of single-dataset parcellations into a 2d-space through multi-dimensional scaling (see methods: Single-dataset parcellations and similarity analysis of parcellations). **c**, Within-dataset reliability of parcellation, calculated as the mean ARI across the 5 levels of granularity (10, 20, 34, 40 and 68 regions). Errorbars indicate SE of the mean across granularity pairs). **d**, Reliability-adjusted ARI between each single-dataset parcellations and the MDTB (task-based) and HCP (resting parcellation) parcellation. Errorbars indicate standard error of the mean across levels of granularity, \*\*  $p < 0.01$ , \*\*\*  $p < 0.0001$ . **e**, DCBC evaluation of the symmetric and asymmetric atlas averaged across granularities evaluated on the group map (left) or on individual maps derived with that atlas (right). **f**, DCBC evaluation of the symmetric group map and of individual maps derived from the model with 10, 20, 34, 40, and 68 regions.

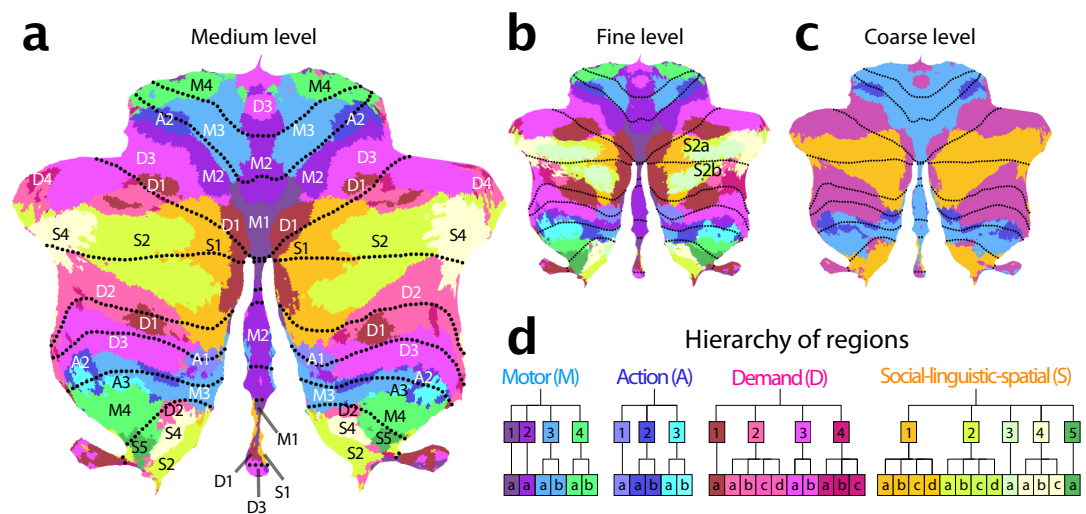


**Figure 2. Cerebellar functional atlas at three levels of granularity.** **a**, Medium granularity with 32 regions; 16 per hemisphere. The colormap represents the functional similarity of different regions (see methods: parcel similarity and clustering). **b**, Fine granularity with 68 regions; 34 per hemisphere. **c**, Coarse granularity with 4 functional domains. The symmetric version of the atlas is shown, for the asymmetric version, see Fig. 4. **d**, Hierarchical organization based on the functional similarity of regions, depicted as a dendrogram. The label of each region indicates the functional domain (M,A,D,S), followed by a region number (1-4), and a lower-case letter for the subregion (a-d).

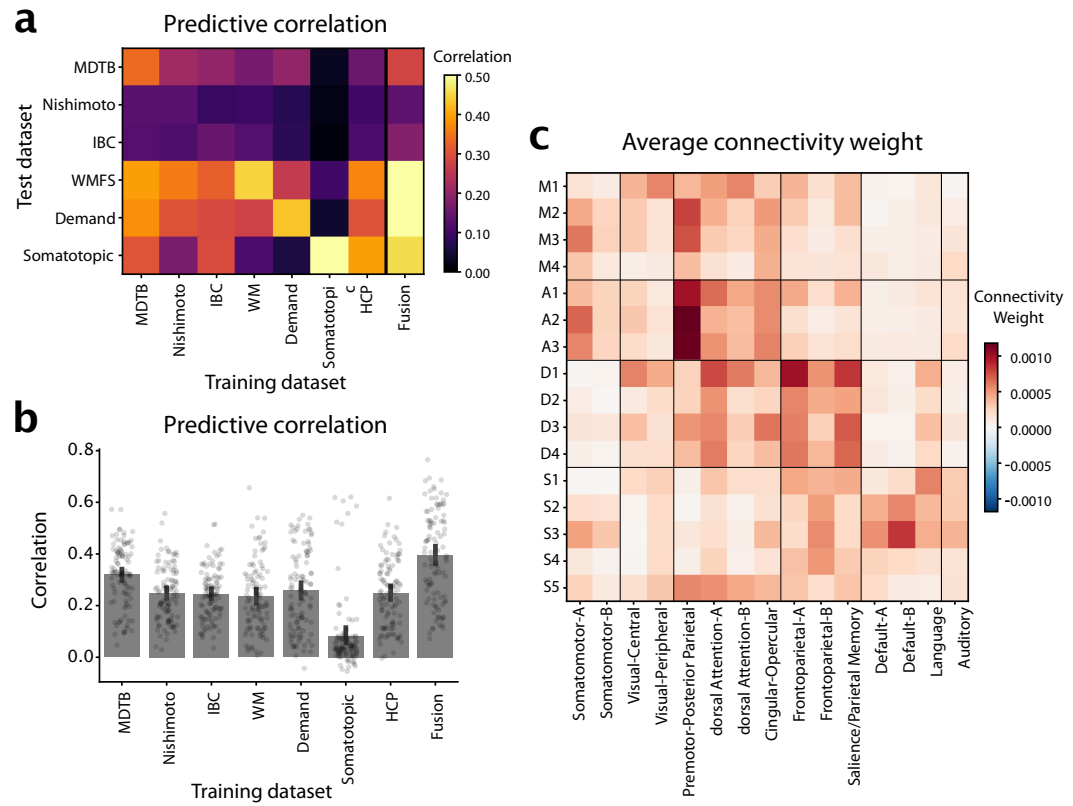


**Figure 3. Cerebro-cerebellar connectivity models.** **a**, Matrix shows the correlation between observed and predicted cerebellar activity patterns for each test dataset (rows). Connectivity models were trained on each training datasets (columns) separately. Evaluation was cross-validated across subjects when training- and test-dataset were identical. **b**, Correlation between observed and predicted activity patterns, averaged across test-datasets. The Fusion model used the average connectivity weights across all task-based datasets (excluding the HCP resting-state data). **c**, Average connectivity weights between each cerebellar region (row), and each of the 15 resting-state networks as described in [29].

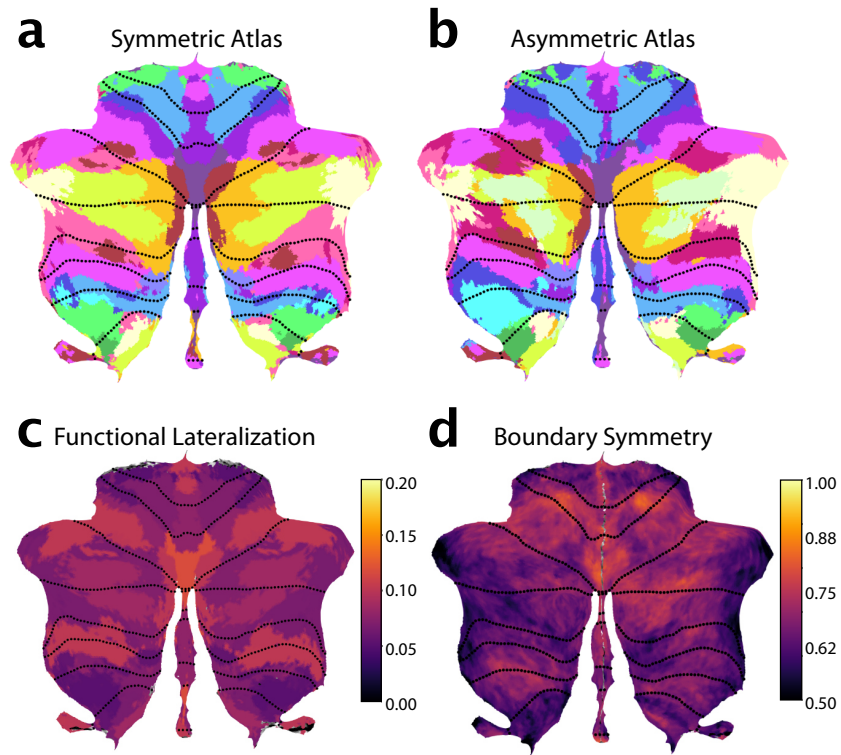


**Figure 4. Functional lateralization and Boundary asymmetry in the cerebellum.** **a**, Symmetric atlas winner-take-all map; **b**, Asymmetric atlas winner-take-all map; **c**, Functional lateralization quantified as the correlations of the functional responses of anatomically corresponding voxel of the left and right hemisphere, averaged across subjects and within each functional region. **d**, Boundary symmetry calculated as the correlations of the probabilistic voxel assignments between the symmetric and asymmetric version of the atlas.

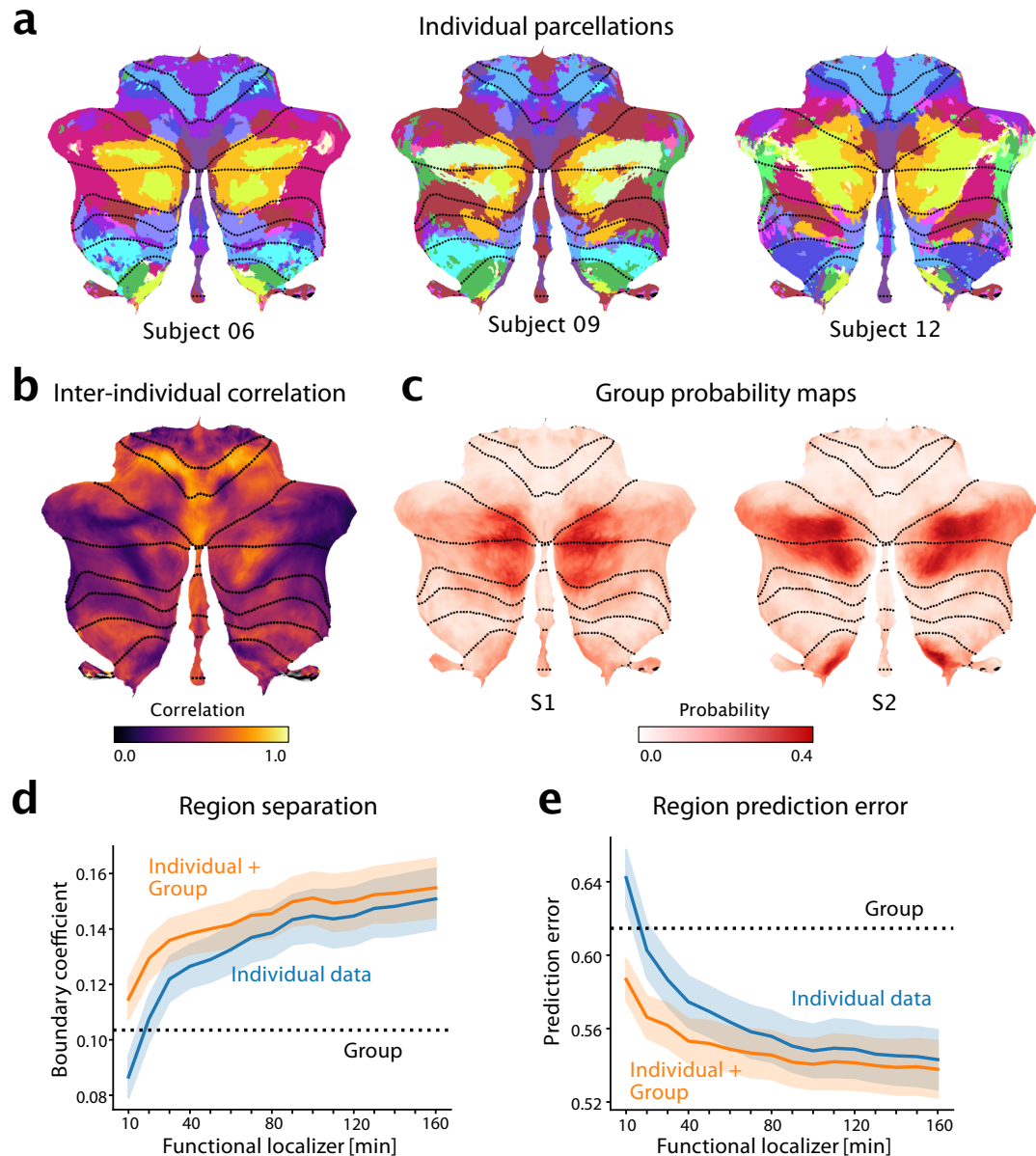


**Figure 5. The functional atlas improves individual precision mapping.** **a**, Individual parcellations from three participants, using 320min of individual data. The region colors correspond to the atlas at medium granularity (32 regions). **b**, Map of the average inter-subject correlations of functional profiles. Correlations are calculated between any pair of subjects in the MDTB dataset, corrected for the reliability of the data (see methods: Inter-individual variability). **c**, Group probability map for regions S1 and S2 (left and right combined) show the overlap of regions. **d**, DCBC evaluation (higher values indicate better performance) on individual parcellations (blue line) derived on 10-160min of individual functional localizing data, compared to group parcellation (dashed line) or the combination of group map and individual data (orange line). **e**, Equivalent analysis using prediction error (see methods, lower is better).



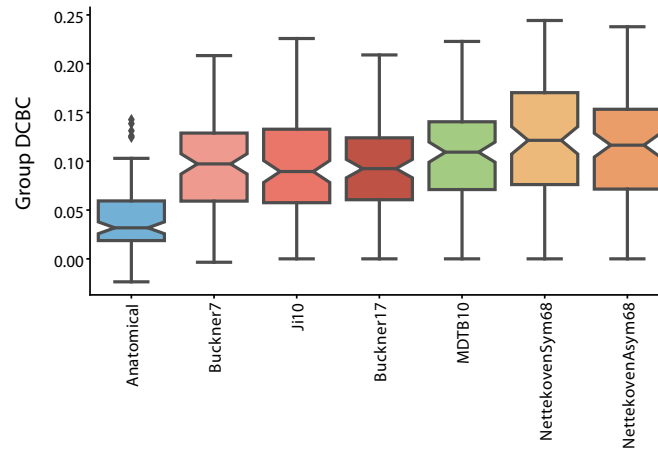


**Figure S1. Fused atlas performance compared to existing atlases.** DCBC evaluation of existing anatomical parcellation (Lobular: [5]), task-based parcellation (MDTB: [3]), and resting-state parcellations (7 and 17 regions: [7]; 10 regions: [6]) averaged across all datasets.

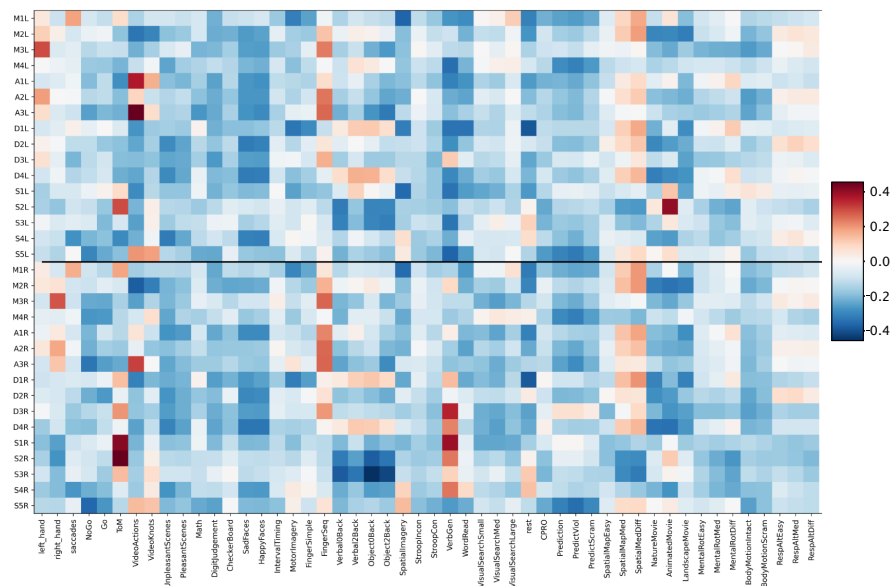


**Figure S2. Functional profiles of regions in MDTB dataset.** Average activity relative to the mean activity in all tasks in MDTB dataset corrected for motor features. Responses were estimated from subject-specific regions and averaged across subjects for visualization. To account for activation that can be explained by the motor aspects of each task, number of movements were used as covariates alongside regressors that coded for each condition separately. Movements were left hand presses, right hand presses and saccades per second.

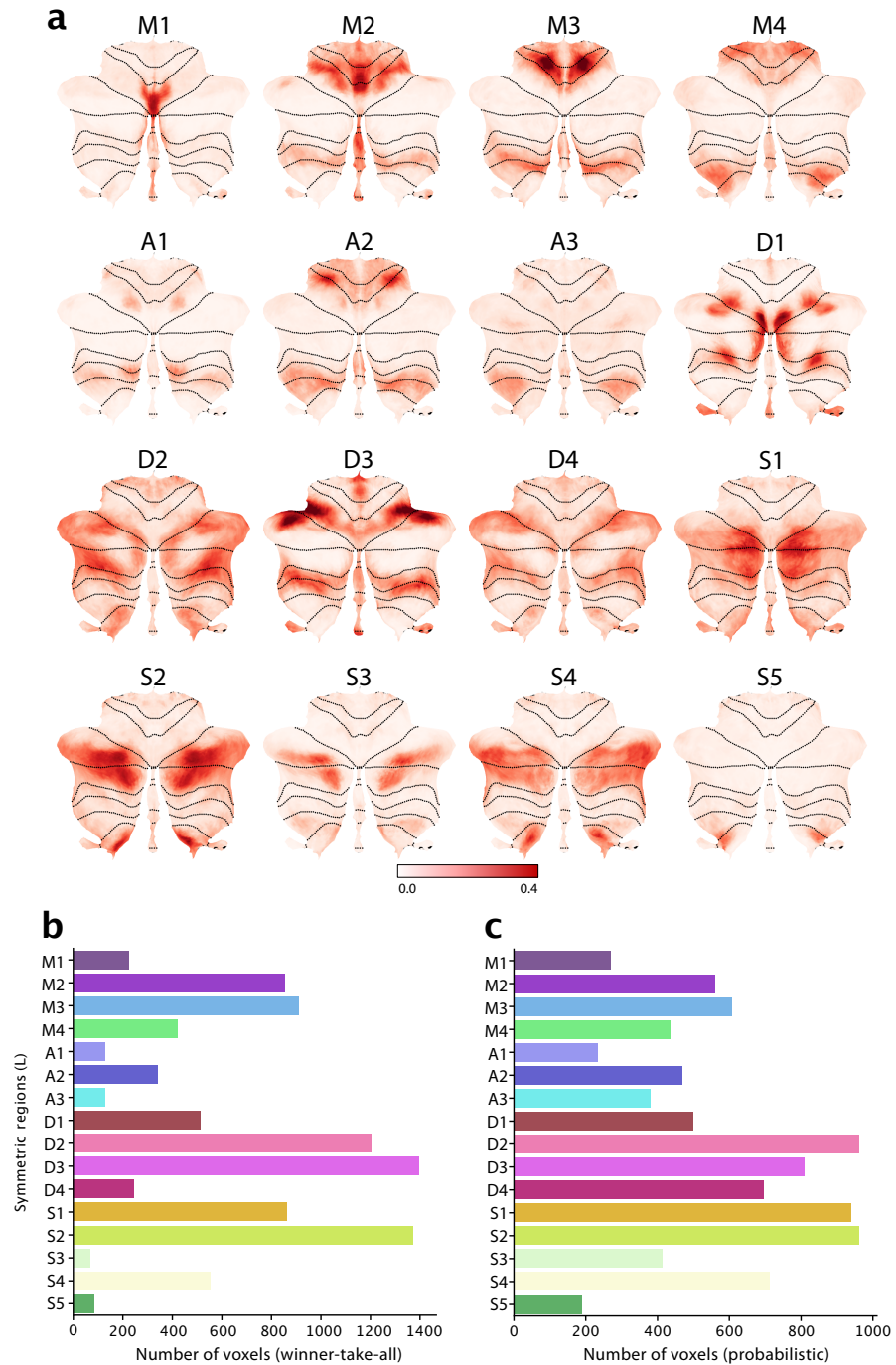


**Figure S3. Probability maps and region size.** **a**, Probability maps for each region displayed on the flat representation. **b**, Size estimate for each region in terms of the number of voxels ( $2\text{mm}^3$ ) using winner-take-all assignment. **c**, Size estimate for each region in terms of the number of voxels ( $2\text{mm}^3$ ) using probabilistic assignments.

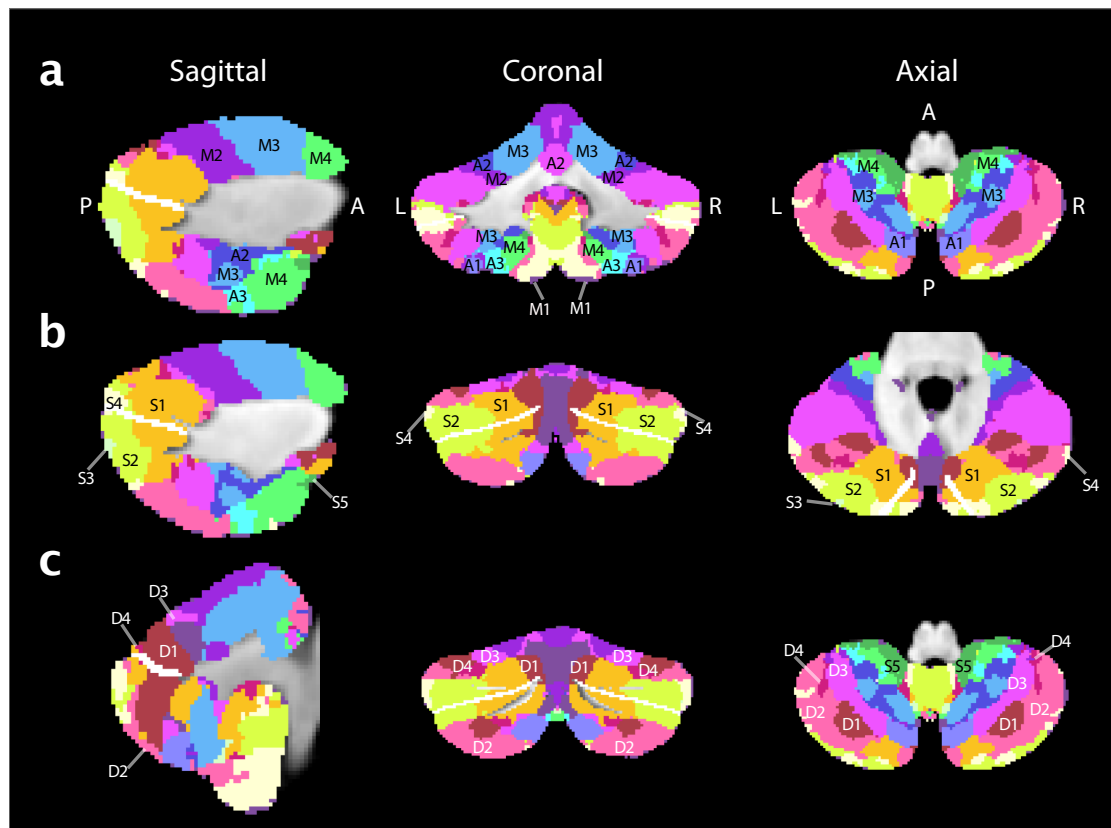


**Figure S4. Atlas in volumetric space.** Atlas shown at medium granularity (32 regions; 16 per hemisphere). Top row shows motor and action regions, middle row shows multi-demand regions and bottom row shows social-linguistic-spatial regions. Horizontal fissure is marked in white.

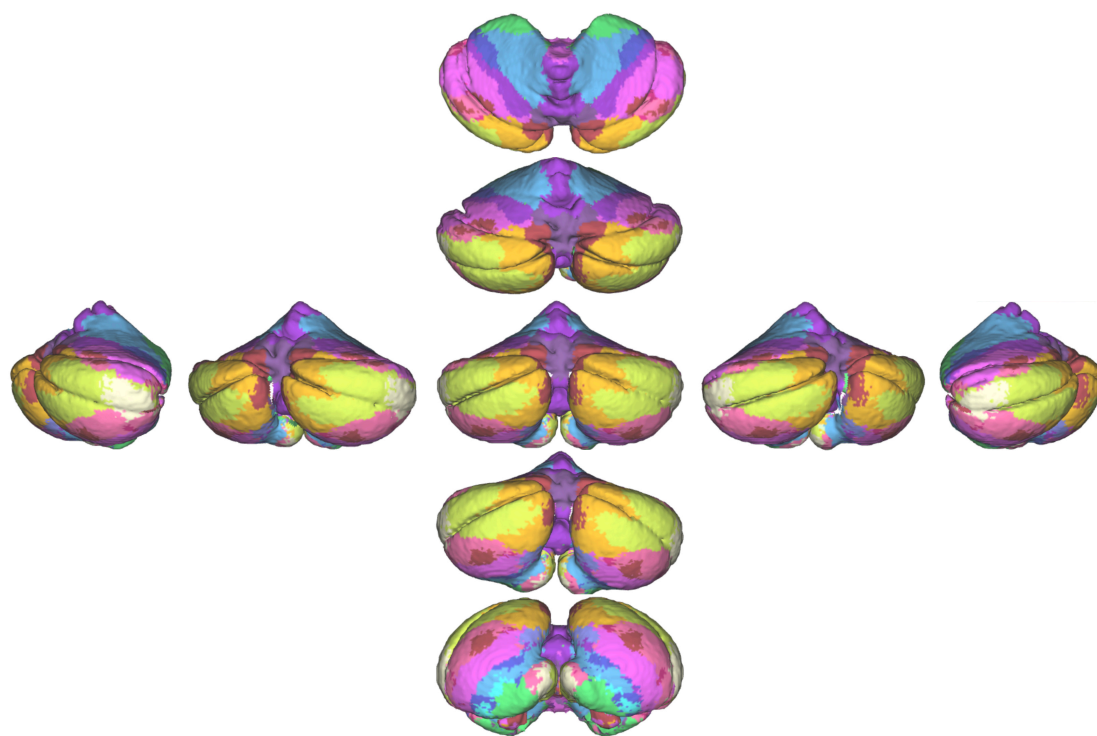


**Figure S5. Atlas in 3D view.** Atlas shown at medium granularity (32 regions; 16 per hemisphere) projected onto the pial surface. The central view is showing the posterior side of the cerebellum. The vertically arranged views show the superior side of the cerebellum at the top and the inferior side at the bottom. The horizontally arranged views show the left and right side of the cerebellum.

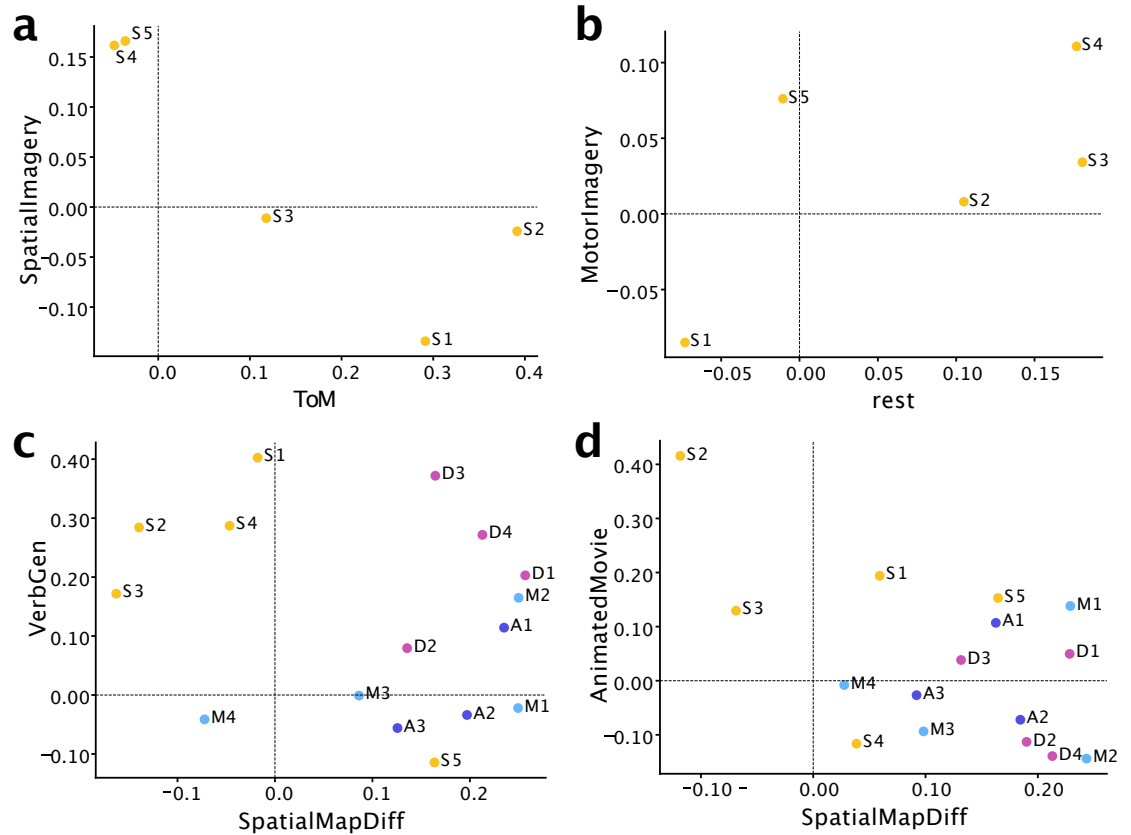


**Figure S6. Regional differences in functional responses for selected tasks.** a-b, Spatial imagery, theory-of-mind, motor imagery and rest separate social-linguistic-spatial (S1-5) regions. c-d, Verb generation, spatial map, and animated movie tasks separate social-linguistic-spatial regions from other domains. For c, only the right regions are shown and for d only the left regions are shown. For the other panels the responses are shown averaged across hemispheres.

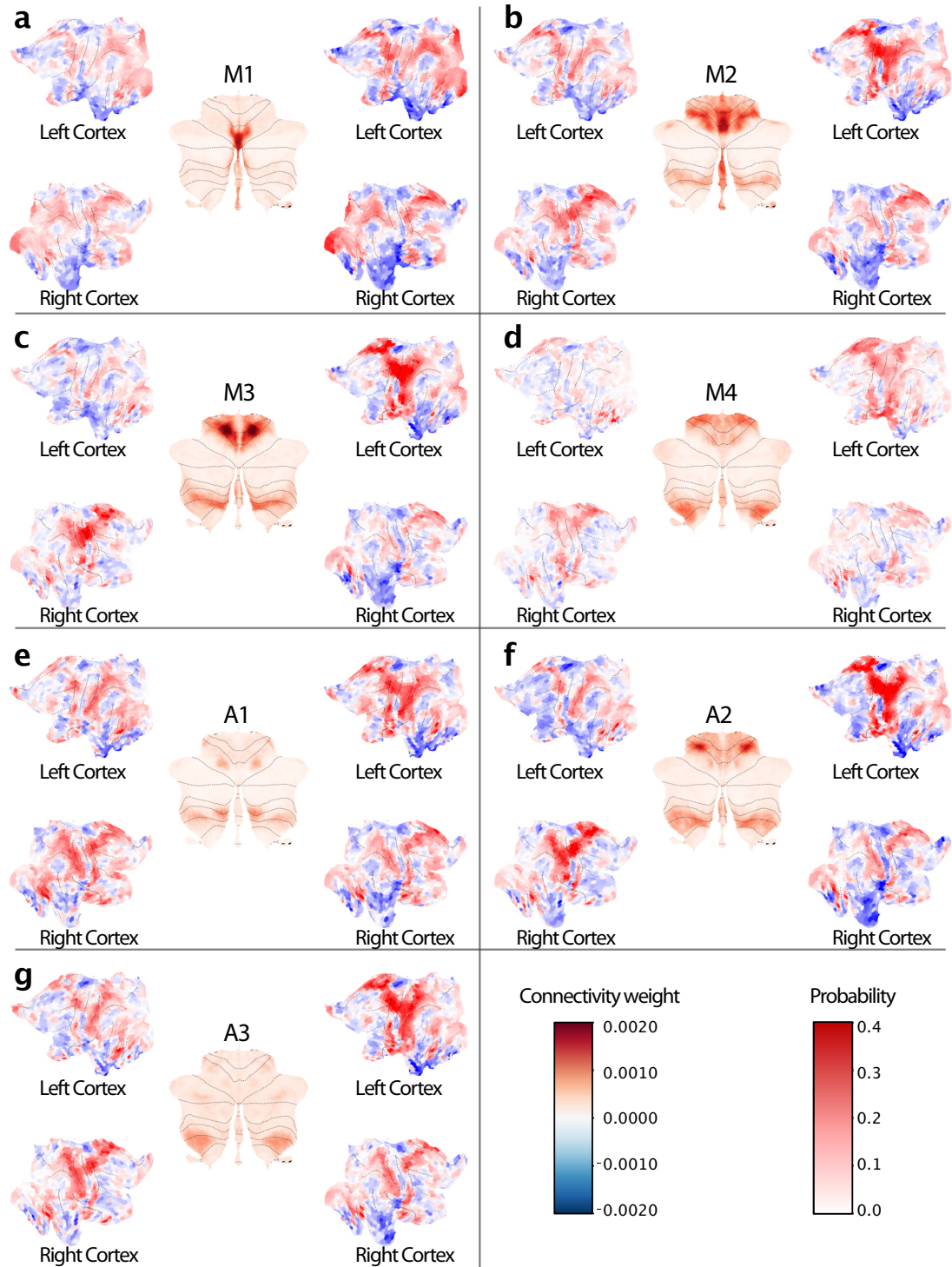


**Figure S7. Cortico-cerebellar connectivity weights and probability maps.** Parcel probability maps for motor (**a-d**) and action (**e-h**) regions are shown in the middle of each figure inset, surrounded by the cortical input weights for the left and right cerebellar parcel. Weights for the left cerebellar parcel are shown to the left of the probability map and for the right cerebellar parcel to the right of each probability map on the cortical flatmap. Motor regions include oculomotor vermis M1 (**a**), tongue and vermal region M2 (**b**), hand M3 (**c**) and lower body M4 (**d**) region. Action regions include spatial simulation regions A1 (**e**), classical action observation A2 (**f**) and motor imagery region A3 (**g**).

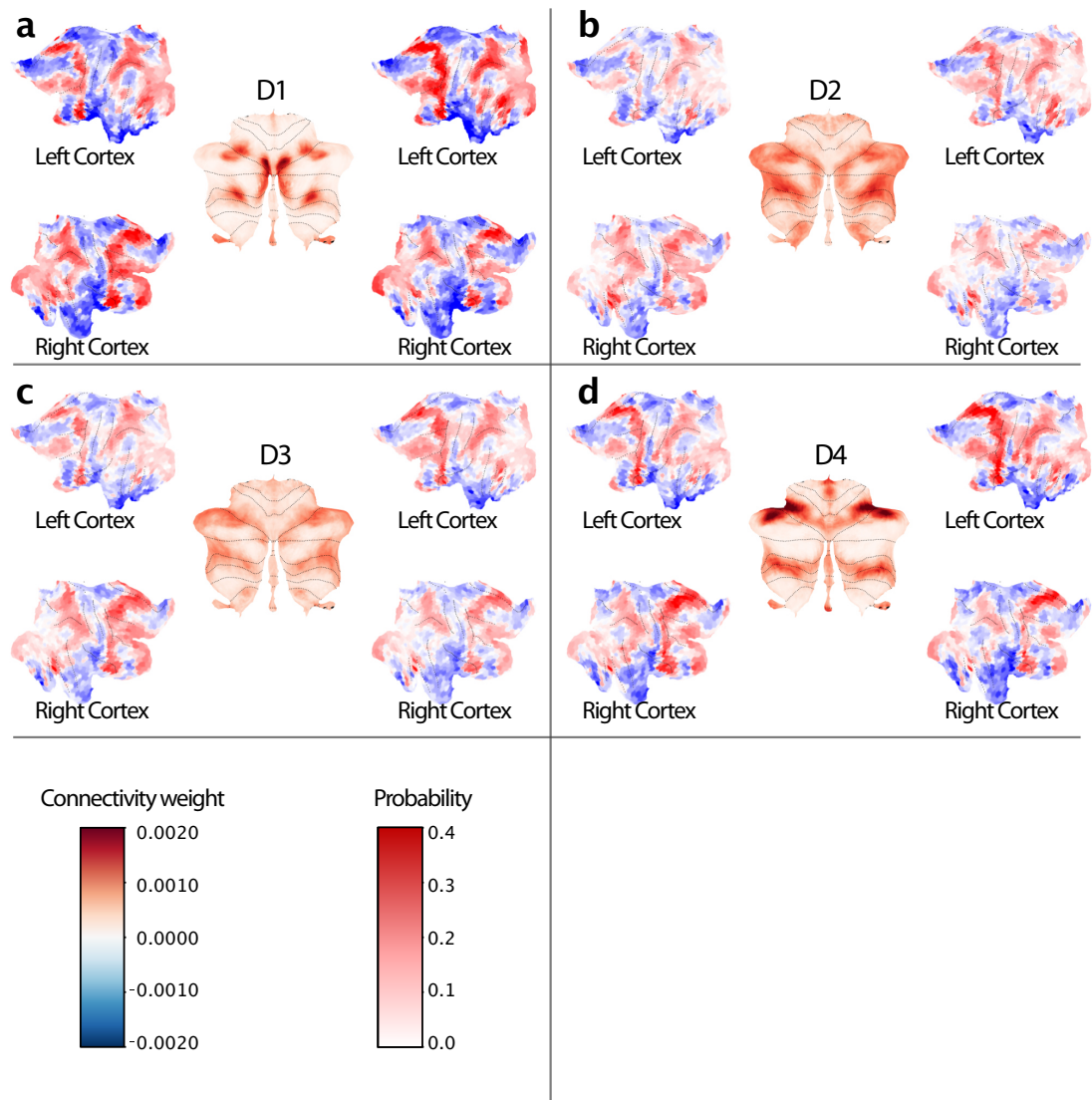


**Figure S8. Cortico-cerebellar connectivity weights and probability maps for demand.** Parcel probability maps for multiple demand (a-d) and social-linguistic-spatial (e-h) regions are shown in the middle of each figure inset, surrounded by the cortical input weights for the left and right cerebellar parcel. Weights for the left cerebellar parcel are shown to the left of the probability map and for the right cerebellar parcel to the right of each probability map on the cortical flatmap. Demand regions include spatial working memory region (a), recall regions (b), difficulty-related (c) and n-back region (d) region.

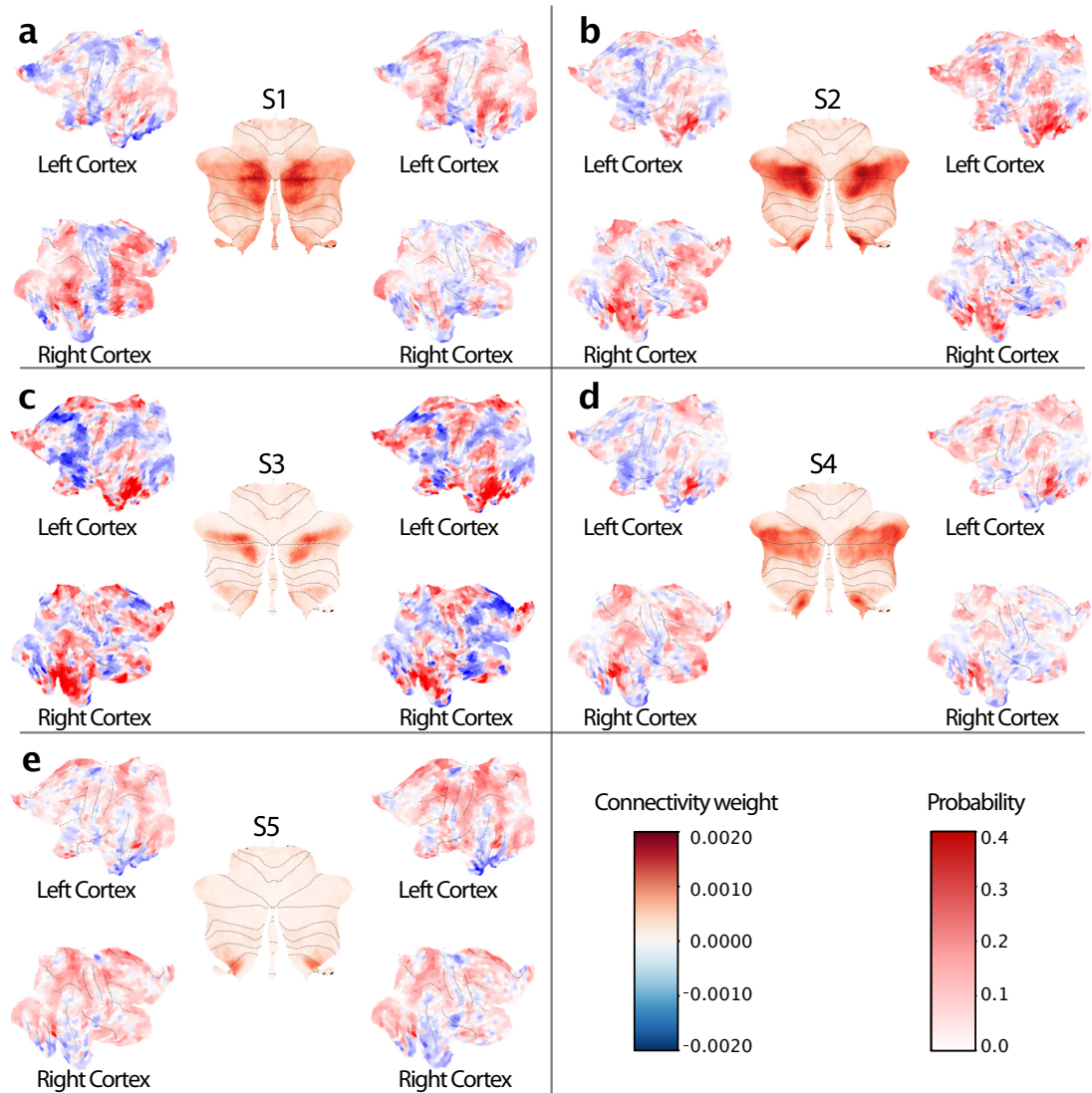


**Figure S9. Cortico-cerebellar connectivity weights and probability maps for social-linguistic-spatial regions.** Parcel probability maps for multiple demand (a-d) and social-linguistic-spatial (e-h) regions are shown in the middle of each figure inset, surrounded by the cortical input weights for the left and right cerebellar parcel. Weights for the left cerebellar parcel are shown to the left of the probability map and for the right cerebellar parcel to the right of each probability map on the cortical flatmap. social-linguistic-spatial regions include linguistic region S1 (a), social region S2 (b), rest region S3 (c), self-projection region S4 (d) and scene construction region S5



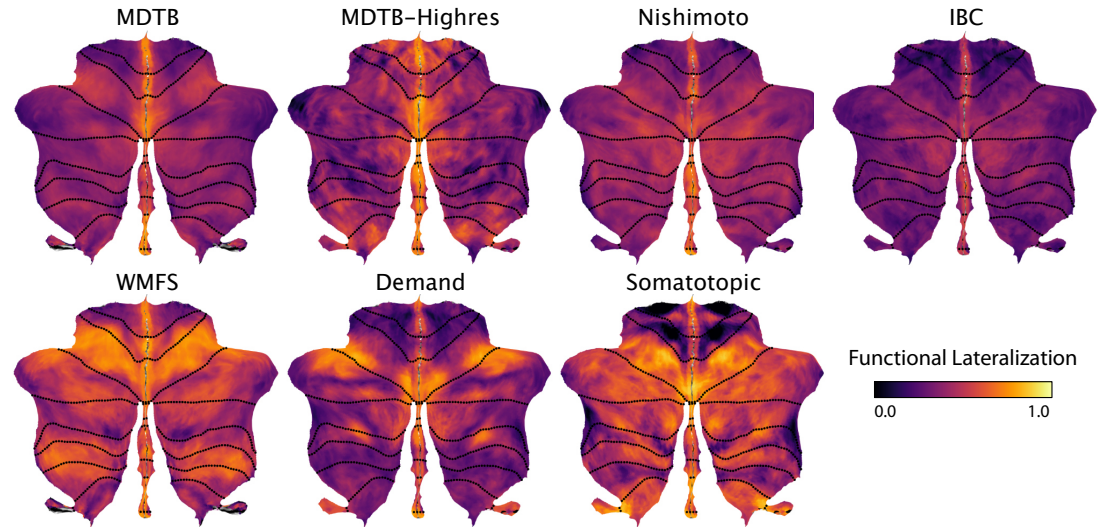


**Figure S10. Individual functional lateralization for each dataset.** Functional lateralization calculated as the correlations of the functional responses of anatomically corresponding voxel of the left and right hemisphere. Functional lateralization was averaged across subjects within each dataset.

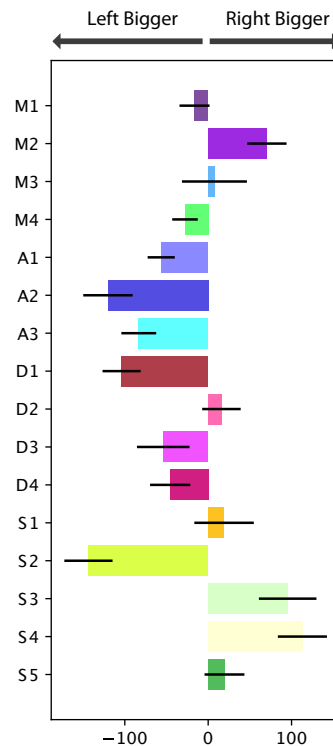


**Figure S11. Size difference between left and right region pairs of the asymmetric atlas.** Regions were estimated in individual subjects using the asymmetric atlas version. The size difference was calculated as number of voxels ( $2mm^3$ ) in right parcel minus number of voxels in left parcel for each individual. Bars show average size difference across individuals and error bars indicate standard error of the mean.